Thin–Walled Structures 208 (2025) 112750

Contents lists available at ScienceDirect

Thin-Walled Structures

journal homepage: www.elsevier.com/locate/tws

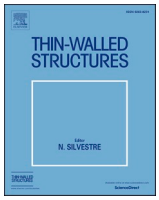

# Microstructure, mechanical properties and cross-sectional behaviour of additively manufactured stainless steel cylindrical shells

Ruizhi Zhang [a,*], Mohsen Amraei [b], Heidi Piili [b], Leroy Gardner [a]

[a] Department of Civil and Environmental Engineering, Imperial College London, London, UK
[b] Department of Mechanical and Materials Engineering, University of Turku, Turku, Finland

ARTICLE INFO

*Keywords:*
Additive manufacturing (AM)
Compression tests
Cylindrical shells
Current design approaches
Digital image correlation (DIC)
Microstructure
Laser scanning
Buckling reduction factor
Powder bed fusion (PBF)
Stainless steel
Tensile coupon tests
3D printing

ABSTRACT

Powder bed fusion is a rapidly developing method of metal additive manufacturing that offers an unprecedented ability to manufacture complex and flexible components with high accuracy. Stainless steel is a high value material that particularly lends itself to the emerging opportunities offered by metal additive manufacturing. There is, however, limited information related to the microstructure, mechanical properties and structural performance of thin-walled stainless steel elements additively manufactured by powder bed fusion; this is addressed in the present study in the context of thin-walled circular shells, which are investigated through a series of physical experiments and numerical simulations. The experimental programme consisted of material coupon tests, microstructural characterisation, geometric measurements and axial compression tests on stainless steel thin-walled cylindrical shells with large diameter-to-thickness ($D/t$) ratios produced by powder bed fusion. Advanced measurement techniques—3D-laser scanning and digital image correlation, were utilised to capture the geometric properties prior to testing and the distribution and development of the deformations and strains during testing, respectively. The measured geometric imperfections in the shells were such that most specimens met the Class A fabrication quality requirements set out in EC3-1-6; all tested shells buckled below their yield loads in an asymmetric chequerboard pattern, showing significant sensitivity to local imperfections. In parallel with the experimental investigation, a numerical modelling programme was carried out, aimed at first replicating the compression tests and then extending the current test data pool over a wider range of slenderness values. The experimental and numerical data were analysed and employed to assess the applicability of existing design methods for conventionally formed tubular sections to those manufactured by powder bed fusion. EC3-1-6 was found to give consistent and safe-sided buckling resistance predictions for the studied stainless steel cylindrical shells under axial compression.

## 1. Introduction

Metal additive manufacturing (AM), commonly known as metal 3D printing, can be used to produce free-form metallic parts layer-by-layer based on a three-dimensional digital model [1–4]. The potential for enhanced geometric freedom, heightened design customisation, reduction in material use and wastage and improved environmental performance [5] over conventional manufacturing techniques, has led to a rapid growth in interest and use in aerospace, automotive and mechanical engineering applications [3,4,6]. According to ISO/ASTM 52900 [7], single-step AM processes for metallic materials are classified into sheet lamination, directed energy deposition (DED) and powder bed fusion (PBF), with the latter two being regarded as the most promising metal AM techniques for use in construction. The PBF process involves the layer-wise deposition and fusion of powdered metals using thermal energy from a laser or electron beam in an enclosed chamber. PBF is synonymous with complex components, with high spatial resolution, low surface roughness, and the ability to print a broad variety of metals. As a high value material, stainless steel has been an extensively studied in the domain of PBF processes over the past few decades, with the material offering a good combination of corrosion resistance and mechanical strength, together with adequate weldability [8,9]. These properties have been demonstrated in a number of previous studies on conventionally produced stainless steel structural elements [10–14]. The primary focus of previous research on PBF stainless steels has been on the identification and suitability of printing parameters, and the

* Corresponding author.
*E-mail address:* ruizhi.zhang@imperial.ac.uk (R. Zhang).

https://doi.org/10.1016/j.tws.2024.112750
Received 24 August 2024; Received in revised form 4 November 2024; Accepted 20 November 2024
Available online 21 November 2024

microstructural and mechanical properties of PBF parts, including austenitic [4,15], ferritic [16], duplex [17] and precipitation-hardening [9] grades. Investigations into the structural performance of PBF stainless steel elements include cross-sectional tests on tubular sections conducted by Zhang et al. [4,19] and Yan et al. [20].

An important challenge to be overcome before additively manufactured structural elements can be applied more widely in the construction industry is the development of structural design guidance, supported by a suitable pool of experimental and numerical data. Circular hollow sections (CHS), a widely used cross-section profile in construction, are known to be prone to buckling under compressive loading, with a high sensitivity to initial geometric imperfections, especially for those with large diameter-to-thickness ratios (commonly referred to as cylindrical shells). The buckling behaviour of conventionally produced steel cylindrical shells has been extensively studied, such as by Seide et al. [21], Newmark and Wilson [22,23] and Zeybek et al. [24,25]. Thick-walled stainless steel CHS additively manufactured by PBF have been investigated in a previous study [4], and thin-walled PBF circular cylindrical shells are examined experimentally and numerically in the present paper from a microstructural, mechanical and cross-sectional perspective. Five cylindrical shells with different diameter-to-thickness $D/t$ ratios were additively manufactured from austenitic 316L stainless steel, while one cylindrical shell was manufactured from martensitic precipitation hardening CX stainless steel. The experimental programme consisted of microstructural characterisation, material coupon tests, initial geometric measurements and compressive stub column tests. Upon successful validation of finite element models against the test results, numerical parametric studies were also conducted to expand the pool of data on PBF stainless steel cylindrical shells. The experimental and numerical results were utilised to evaluate the applicability of existing design approaches for conventionally formed sections to additively manufactured stainless steel tubular sections.

## 2. Specimen manufacture

Five circular cylindrical shells with nominal cross-section sizes (outer diameter $D$ × thickness $t$) of C150 × 1.0, C180 × 1.0, C150 × 0.7, C180 × 0.7 and C200 × 0.7, were manufactured by laser-based powder bed fusion (L-PBF) using 316L stainless steel powder. One circular cylindrical shell with a nominal outer diameter $D$ of 200 mm and thickness $t$ of 1.0 mm (C200 × 1.0), was also produced by L-PBF using CX stainless steel powder. Both stainless steel grades, which are well-suited to PBF additive manufacturing, were examined in the current study in order to cover both normal-strength (316L) and high-strength (CX) stainless steels, enabling a comprehensive analysis of the local buckling behaviour of PBF stainless steel cylindrical shells under axial compression. All examined cross-sections are classed as slender (Class 4) according to EN 1993-1-4 [26]. The nominal chemical composition of the adopted austenitic grade 316L stainless steel (also referred to as EN 1.4404 and X2CrNiMo17-12-2) and martensitic precipitation hardening (PH) grade CX stainless steel (with similar chemical composition to PH 13-8 Mo) is provided in Table 1. Fresh gas-atomised stainless steel powder from EOS GmbH with a nominal particle size distribution of 15–53 μm [27] and 20–65 μm [28] for the 316L and CX stainless steels respectively, were used as the raw material.

All the shells and coupons were manufactured using an EOS M 290 PBF machine, featuring a 250 mm × 250 mm × 325 mm building envelope and a Yb-fibre laser, in the Department of Mechanical Engineering at LUT University. Prior to manufacturing, the substrate was preheated to 80 °C to reduce the residual stress in the specimens. The manufacturing process involved the laser beam repeatedly scanning across the programmed locations defined by an input STL model, melting the powder onto the existing solidified layers until final completion of the target part. During fabrication, high-purity nitrogen was maintained in the chamber to avoid oxidation of the specimens. A support structure was printed to constrain each specimen during the build and to reduce the distortion induced by the removal of the build plate. Following fabrication, no thermal stress relief or other post-processing was conducted except removing from the build plate using a bandsaw, grinding off the support structures and machining off the specimen ends. Photographs of a typical test specimen during and after printing, along with its removal from the build plate are shown in Fig. 1. The detailed L-PBF processing parameters, including laser power, focal point diameter of the laser, scanning speed, layer thickness, hatch distance, protective gas, etc., were set by the EOS machine manufacturer, as provided in Table 2. A bi-directional stripe hatching strategy with interlayer rotations of 47° for 316L and 67° for CX was adopted during printing, as illustrated in Fig. 2. Photographs of the examined L-PBF 316L stainless steel cylindrical shell specimens are shown in Fig. 3.

Fig. 4 illustrates the build orientation of the printed coupons, the coupon dimensions, which were in compliance with EN ISO 6892-1 [29], and the extracted positions of the metallurgic samples from the coupons. The reference coordinates for the L-PBF coupons consist of three perpendicular axes: the build direction (BD) and the two transverse directions (TD1 and TD2). The build orientation angles of the tensile coupons are defined by three parameters, $\theta$, $\psi$ and $\phi$, where $\theta$ is the angle from the longitudinal axis of the coupon to the build plate (i.e. $\theta = 0°$ is a horizontal coupon parallel to the build plate and $\theta = 90°$ is a vertical coupon), $\psi$ is the angle between the recoating direction (i.e. TD2 axis) and the longitudinal axis of the coupon (with $\psi = 90°$ for all $\theta = 90°$ coupons) and $\phi$ is the angle between the long face of the coupon cross-section and the build plate. For the vertical coupons ($\theta = 90°$), $\phi = 0°$ is a coupon with the short face of its cross-section parallel to the recoating direction, and $\phi = 90°$ is a coupon with its long face parallel to the recoating direction.

## 3. Tensile testing

Eighteen uniaxial tensile coupon tests were conducted to ascertain the mechanical properties of the examined L-PBF stainless steel on the macroscopic scale. All the tests, including the compression tests described in Section 6, were carried out in the Structures Laboratory of the Department of Civil and Environmental Engineering at Imperial College London. Prior to testing, the width and thickness of the parallel section of each coupon were measured, and standard gauge lengths of $5.65\sqrt{S_0}$ [29], where $S_0$ is the original cross-sectional area of the parallel length, were scribed onto both coupon faces for the post-test calculation of fracture strains.

An overview of the tensile coupon test setup is shown in Fig. 5. The material tests were performed in compliance with EN ISO 6892-1 [29], using an Instron 8802 250 kN hydraulic testing machine. The testing machine was driven under displacement control, with crosshead separation rates being determined to achieve a strain rate of 0.007 % $s^{-1}$ up to the 0. 2% proof stress and of 0.025 % $s^{-1}$ beyond yielding and a gradual ramp between them. A four-camera LaVision digital image correlation (DIC) system was employed to capture the surface deformations and hence strains over the parallel length on the front and back faces of each coupon, which were spray painted with a matte white

**Table 1**
Nominal chemical composition of the adopted stainless steel powder (in wt.%), as provided by the manufacturer [27,28].

| Stainless steel | Cr | Ni | Mo | Al | C | Mn | Cu | P | S | Si | N | Fe |
|---|---|---|---|---|---|---|---|---|---|---|---|---|
| 316L | 17.00–19.00 | 13.00–15.00 | 2.25–3.00 | – | ≤0.03 | ≤2.00 | ≤0.50 | ≤0.025 | ≤0.01 | ≤0.75 | ≤0.10 | balance |
| CX | 11.00–13.00 | 8.40–10.00 | 1.10–1.70 | 1.20–2.00 | ≤0.05 | ≤0.40 | – | – | – | ≤0.40 | – | balance |

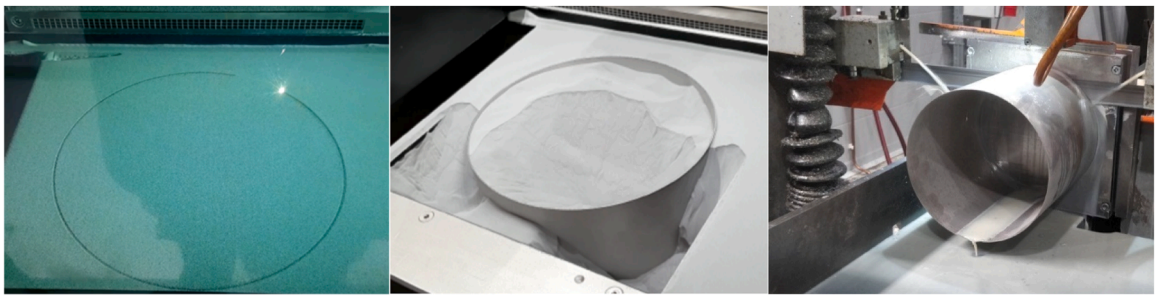


**Fig. 1.** Typical test specimen (a) during printing, (b) after printing and (c) being removed from the build plate.

**Table 2**
PBF processing parameters adopted in this study.

| Stainless steel | Laser power (W) | Focal point diameter (μm) | Scanning speed (mm/s) | Volume rate ($mm^3/s$) | Layer thickness (μm) | Hatch distance (μm) | Scanning rotation (°) | Preheated powder bed (°C) | Preheated powder | Shielding gas |
|---|---|---|---|---|---|---|---|---|---|---|
| 316L | 214.2 | 70–80 | 928.1 | 3.7 | 40 | 100 | 47 | 80 | No | Argon |
| CX | 260.0 | 100 | 1000.0 | 3.2 | 30 | 100 | 67 | 80 | No | Argon |

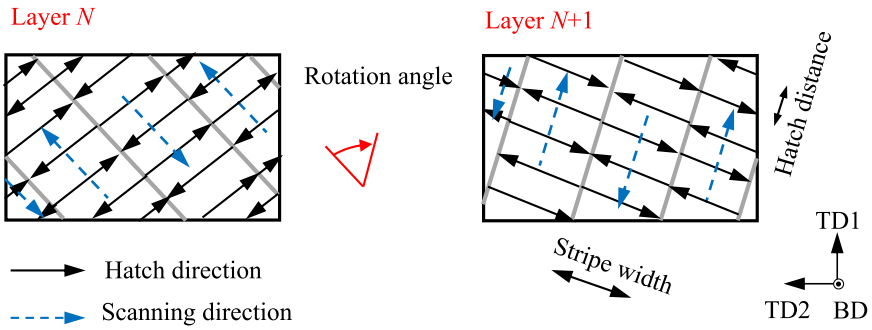


**Fig. 2.** Schematic illustration of the adopted stripe scanning strategy.

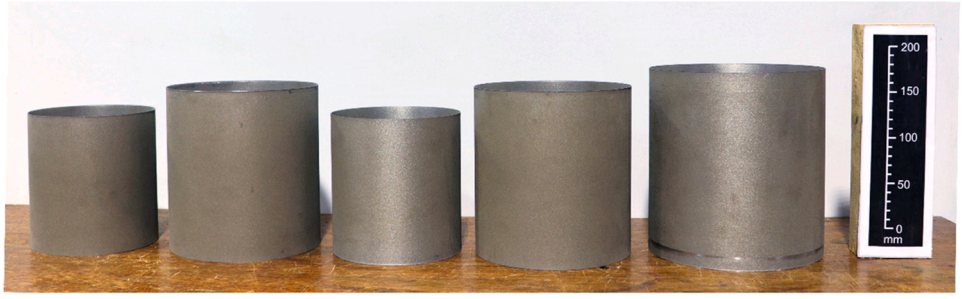


**Fig. 3.** Photograph of all PBF 316L stainless steel shell specimens (with increasing slenderness from left to right).

background and a random black speckle pattern of high contrast prior to testing. The applied forces were measured using a load cell within the testing machine and fed into the DIC system via an analogue to digital converter, at 1-second intervals. The acquired DIC images were recorded at 1-second intervals and post-processed using Davis 10 [30].

The measured engineering stress-strain curves obtained from the 316L and CX stainless steel coupons are plotted in Figs. 6 and 7, respectively, while the key material properties, including the Young's modulus $E$, 0.2 % proof strength $\sigma_{0.2}$, 1.0 % proof strength $\sigma_{1.0}$, ultimate tensile strength $\sigma_u$ and corresponding strain $\varepsilon_u$, fracture strain over the marked gauge length $\varepsilon_f$, Ramberg–Osgood parameter $n$ [31] and extended strain hardening parameters $m_{1.0}$ and $m_u$ [32,33], which were fitted to the measured stress-strain curves using the methods provided in [34,35], are summarised in Tables 3 and 4. The stress-strain curves derived from the Ramberg-Osgood parameters are also shown in Figs. 6 and 7 for the 316L and CX stainless steels, respectively.

The mechanical properties measured in this study are comparable to those provided by the manufacturer, as reported in Table 5 [27,28]. The L-PBF 316L stainless steel was found to have a good balance of strength and ductility, considering the strength-ductility trade-off seen in equivalent conventionally manufactured material—see Fig. 8 [36,37] and Table 5; this observation is aligned with other studies on 316L stainless steel produced by L-PBF using optimised parameters [38,39]. Some mechanical anisotropy was observed in the tested L-PBF 316L

Building orientation angles (°)

| Coupon | $\theta$ | $\psi$ | $\phi$ |
|---|---|---|---|
| 316L-1~316L-3 | 90 | 90 | 0 |
| 316L-4~316L-6 | 90 | 90 | 90 |
| 316L-7~316L-9 | 0 | 0 | 0 |
| 316L-10~316L-12 | 0 | 0 | 90 |
| CX1~CX6 | 0 | 0 | 90 |

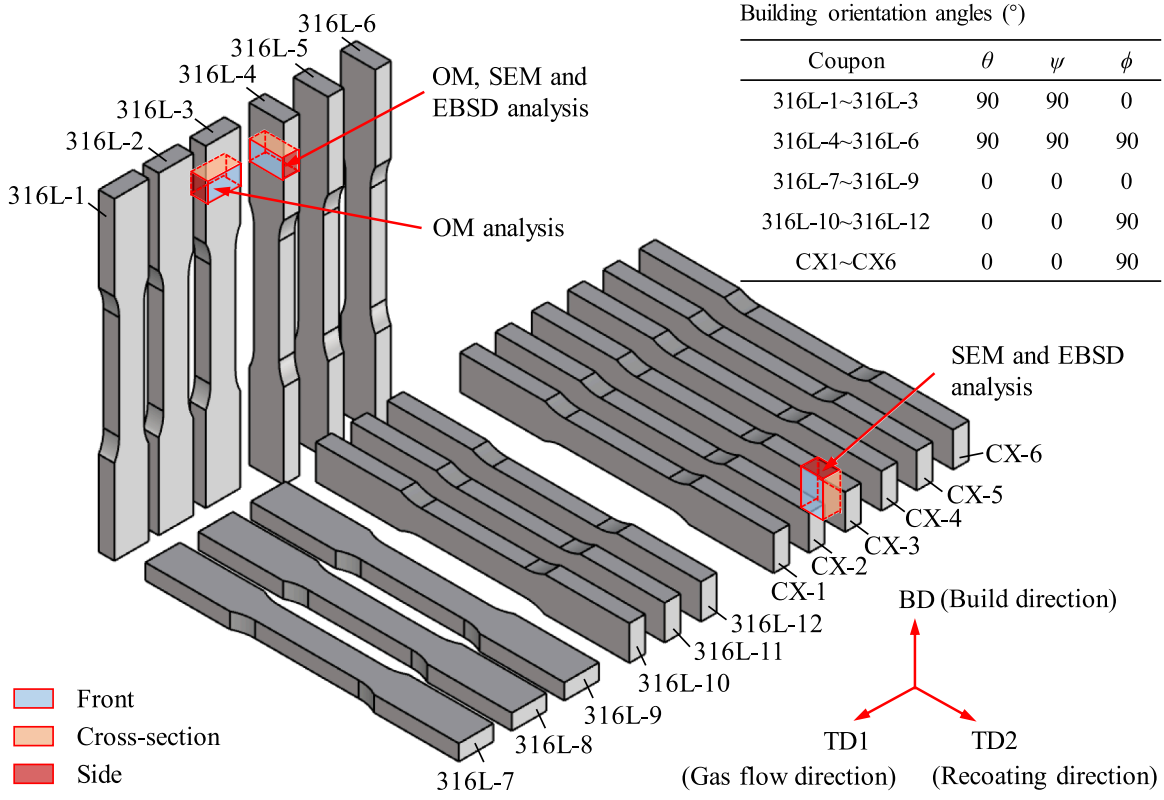


**Fig. 4.** (a) Schematic illustration of the printed coupons, showing the building orientation angles and the extracted positions of the metallurgical sample, and (b) dimensions of each coupon (in mm). The sections used for microstructural observations have been marked in red.

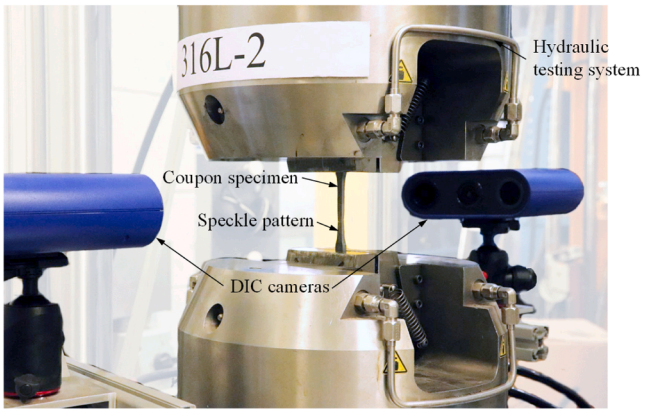


**Fig. 5.** Tensile coupon test setup.

stainless steel, though not to the same extent as found in previous studies on wire arc additively manufactured (WAAM) stainless steel [40]. The horizontal coupons ($\theta = 0°$) showed higher proof stresses ($\sigma_{0.2}$ and $\sigma_{1.0}$) and ultimate stresses $\sigma_u$ but substantially lower ultimate strains $\varepsilon_u$ and fracture strains $\varepsilon_f$, compared to the vertical coupons ($\theta = 90°$); this material anisotropy will be explained in Section 4.2. The strength-ductility balance of the tested L-PBF and CX stainless steel, in comparison with equivalent conventionally produced material with and without heat treatment is summarised graphically in Fig. 9 [9,41–45]. The good combination of strength and ductility of the as-built CX stainless steel in this study supports the suitability of the adopted printing parameters. The L-PBF CX stainless steel in the as-built and heat treatment conditions exhibited higher 0.2 % proof stresses and comparable fracture strains compared to their wrought counterparts. The L-PBF CX stainless steels in the aged and solution-aged conditions had higher 0.2 % proof stresses at the expense of ductility.

## 4. Correlation between microstructure and mechanical properties

### 4.1. Employed techniques and methods

After the destructive material tests, small metallurgical samples were extracted from the gripped sections of the fractured coupons, with three

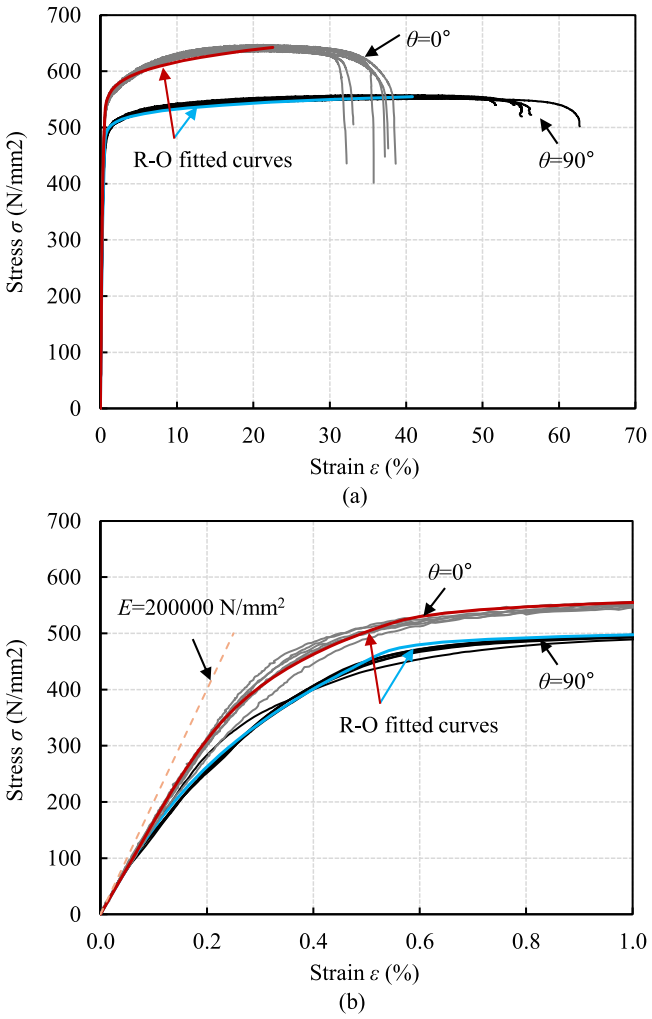


**Fig. 6.** (a) Full range and (b) initial range of stress-strain curves obtained from tensile coupon tests on L-PBF 316L stainless steel.

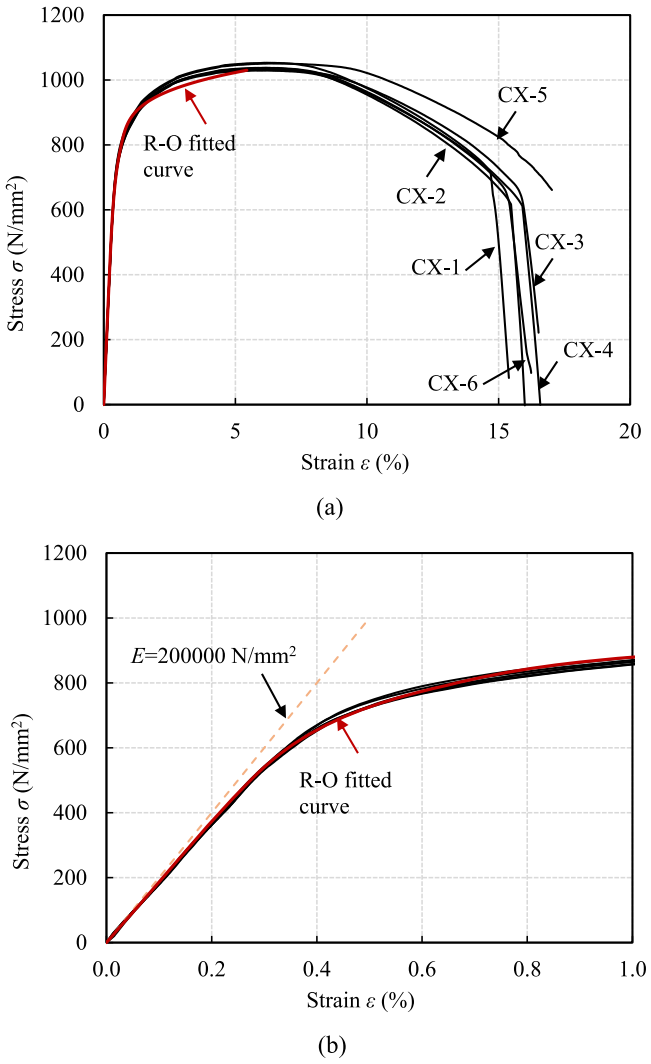


**Fig. 7.** (a) Full range and (b) initial range of stress-strain curves obtained from tensile coupon tests on L-PBF CX stainless steel.

faces (parallel to three orthogonal planes TD2-BD, TD1-TD2 and TD1-BD) being observed, as shown in Fig. 4. The samples were prepared for microstructural characterisation in accordance with ASTM E3-11 [46]. The samples were mounted in bakelite, ground with silicon carbide paper (progressing from 500, 800, 1200 to 2000 grit) and polished to a mirror finish, using 6 μm and 1 μm diamond suspensions and finally a mixture of OP-S colloidal silica solution (OP-S:$H_2O_2$:$H_2O$ = 7:3:10). The polished samples were then electrolytically etched using 10 % wt. oxalic acid solution at 6 volts for around 45 seconds, as recommended by ASTM E407-07 [47] to reveal the solidification structure. The sample preparation and optical microscopy were performed in the Engineering Alloys Lab, while the SEM and EBSD were conducted in the Harvey Flowers Electron Microscopy Suite, both in the Department of Materials at Imperial College London.

The etched surfaces were first observed under an Olympus BX51 optical microscope. The grain size and morphology, texture and crystal phases were investigated using an FEI Quanta 650 SEM equipped with a Bruker eFlash$^{HD}$ EBSD detector and Argus forescatter diodes (FSD) imaging. The stainless steel samples for EBSD were tilted to 70° relative to the horizontal to generate patterns of sufficient intensity. The aperture size, working distance, detector distance and accelerating voltage used to collect the data were 100 μm, 15 mm, 18 mm and 20 kV, respectively. The surfaces of the 316L and CX stainless steel samples were scanned at magnifications of 300× and 4000× over an area of 1427 × 936 μm$^2$ and 104 × 70 μm$^2$, respectively. The 316L stainless steel sample in the TD1-TD2 plane was scanned at 500× magnification to avoid losing substructure details while ensuring enough grains over a large area. The EBSD patterns were acquired using Esprit 2.2 acquisition software [48] and reconstructed through grain dilution and segmentation using the Matlab toolbox MTEX 5.6.0 [49]. The particle size distribution of the L-PBF stainless steel CX was measured using a laser diffraction particle machine (Malvern Mastersizer 2000) in the Centre for Infrastructure Materials of the Department of Civil and Environmental Engineering at Imperial College London.

### 4.2. *Microstructural characterisation of L-PBF 316L stainless steel*

The microstructure of samples extracted from the 316L-3 and 316L-4 coupons was inspected in the TD1-BD, TD2-BD and TD1-TD2 planes; the samples extracted from the 316L-4 coupon were also characterised through EBSD. Fig. 10 shows optical micrographs of the three principal planes of the observed L-PBF 316L stainless steel samples. Periodic melt pools, which were generated by the scanning laser beam, were observed in the TD1-BD and TD2-BD planes and mosaic structures (a cross-like arrangement) were seen in the TD1-TD2 plane due to the interlayer rotation. The melt pool boundaries can be clearly observed in the SEM micrographs (see Fig. 11), and the width and height of the melt pool perpendicular and along the laser beam direction were measured to be around 145 μm and 75 μm, respectively. At higher magnifications, fine

**Table 3**
Measured material properties from tensile coupon tests.

| Coupon | $\theta$ (°) | $E$ (N/mm$^2$) | $\sigma_{0.2}$ (N/mm$^2$) | $\sigma_{1.0}$ (N/mm$^2$) | $\sigma_u$ (N/mm$^2$) | $\varepsilon_u$ (%) | $\varepsilon_f$ (%) | $n$ | $m_{1.0}$ | $m_u$ |
|---|---|---|---|---|---|---|---|---|---|---|
| 316L-1 | 90 | 164800 | 434.0 | 499.7 | 554.0 | 42.7 | 60.7 | 2.7 | 6.4 | 7.1 |
| 316L-2 | 90 | 162000 | 424.1 | 496.8 | 552.5 | 47.2 | 62.0 | 5.0 | 7.2 | 8.2 |
| 316L-3 | 90 | 171300 | 422.4 | 498.7 | 553.5 | 40.8 | 59.3 | 2.7 | 7.1 | 7.9 |
| 316L-4 | 90 | 169700 | 433.3 | 502.8 | 556.7 | 39.7 | 59.0 | 2.7 | 6.6 | 7.5 |
| 316L-5 | 90 | 170500 | 435.3 | 504.6 | 558.9 | 37.2 | 58.5 | 2.6 | 6.4 | 6.9 |
| 316L-6 | 90 | 163900 | 437.3 | 502.5 | 554.2 | 37.2 | 60.5 | 3.0 | 6.3 | 6.7 |
| 316L-7 | 0 | 162100 | 505.8 | 556.9 | 637.1 | 23.0 | 34.9 | 7.5 | 3.5 | 4.2 |
| 316L-8 | 0 | 163900 | 502.8 | 562.2 | 641.9 | 21.5 | 33.6 | 5.4 | 3.8 | 4.3 |
| 316L-9 | 0 | 167500 | 515.0 | 565.6 | 647.3 | 21.3 | 37.3 | 5.5 | 3.3 | 3.8 |
| 316L-10 | 0 | 164800 | 512.5 | 556.8 | 643.8 | 23.1 | 37.1 | 8.3 | 3.0 | 3.9 |
| 316L-11 | 0 | 168800 | 500.8 | 556.0 | 639.0 | 22.4 | 39.0 | 5.0 | 3.5 | 4.0 |
| 316L-12 | 0 | 164600 | 490.0 | 558.9 | 645.8 | 23.9 | 38.2 | 3.6 | 4.0 | 4.6 |
| Average | 90 | 167000 | 431.1 | 500.8 | 555.0 | 40.8 | 60.0 | 3.1 | 6.7 | 7.4 |
| | 0 | 165300 | 504.5 | 559.4 | 642.5 | 22.5 | 36.7 | 5.9 | 3.5 | 4.1 |

**Table 4**
Measured material properties from horizontal ($\theta = 0°$) tensile coupon tests.

| Coupon | $E$ (N/mm$^2$) | $\sigma_{0.2}$ (N/mm$^2$) | $\sigma_{1.0}$ (N/mm$^2$) | $\sigma_u$ (N/mm$^2$) | $\varepsilon_u$ (%) | $\varepsilon_f$ (%) | $n$ | $m_{1.0}$ | $m_u$ |
|---|---|---|---|---|---|---|---|---|---|
| CX-1 | 186300 | 798.4 | 938.4 | 1053.1 | 6.2 | 15.9 | 8.2 | 3.1 | 3.6 |
| CX-2 | 187300 | 771.3 | 917.9 | 1036.7 | 6.2 | 20.2 | 7.8 | 3.1 | 3.7 |
| CX-3 | 186700 | 777.5 | 926.9 | 1032.4 | 6.0 | 20.8 | 7.1 | 3.3 | 3.8 |
| CX-4 | 187200 | 777.5 | 926.1 | 1029.0 | 5.8 | 21.2 | 7.7 | 3.4 | 3.9 |
| CX-5 | 187300 | 788.9 | 931.6 | 1050.9 | 6.4 | 21.7 | 8.9 | 3.2 | 3.8 |
| CX-6 | 186600 | 773.6 | 921.9 | 1037.8 | 6.1 | 21.1 | 7.8 | 3.2 | 3.7 |
| Average | 186900 | 781.2 | 927.1 | 1040.0 | 6.1 | 20.2 | 7.9 | 3.2 | 3.7 |

**Table 5**
Summary of material properties of 316L and CX stainless steel.

| Material | Condition | Source | $\theta$ (°) | $E$ (N/mm$^2$) | $\sigma_{0.2}$ (N/mm$^2$) | $\sigma_u$ (N/mm$^2$) | $\varepsilon_f$ (%) |
|---|---|---|---|---|---|---|---|
| 316L | L-PBF | EOS datasheet [27] | 0 | 185000 | 470–590 | 590–690 | 25–55 |
| | | | 90 | 180000 | 380–560 | 485–595 | 30–70 |
| | L-PBF | Bartolomeu et al. [38] | – | – | 486 | 630 | 25 |
| | Cast | Bartolomeu et al. [38] | – | – | 198 | 450 | 45 |
| | Hot pressing | Bartolomeu et al. [38] | – | – | 293 | 571 | 34 |
| | Wrought | Mower & Long [18] | | 187000 | 345 | 563 | 30 |
| CX | L-PBF | EOS datasheet [28] | – | – | 840 | 1080 | 14.0 |
| | L-PBF | Yan et al. [9] | 0 | – | 694 | 1043 | 16.3 |
| | Wrought | Wu et al. [41] | – | – | 817 | 1107 | 8.3 |

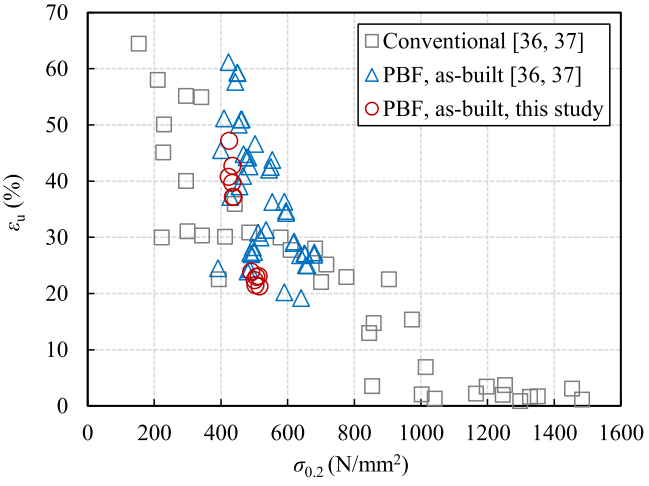


**Fig. 8.** Summary of strain at ultimate stress versus 0.2% proof stress for 316L stainless steel, reproduced from Refs. [36,37].

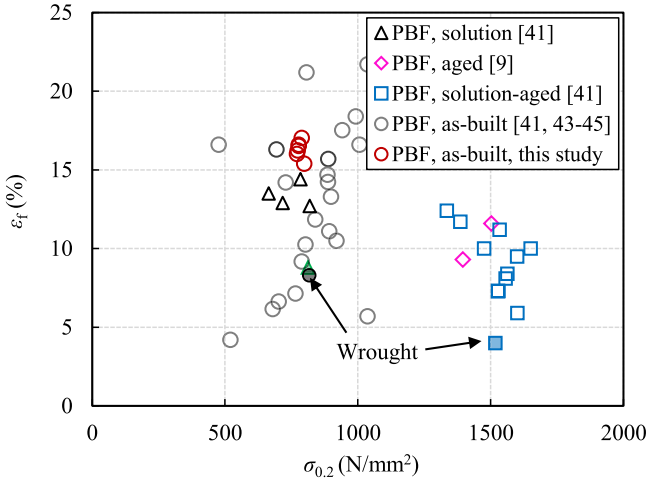


**Fig. 9.** Summary of fracture strain versus 0.2% proof stress for CX stainless steel.

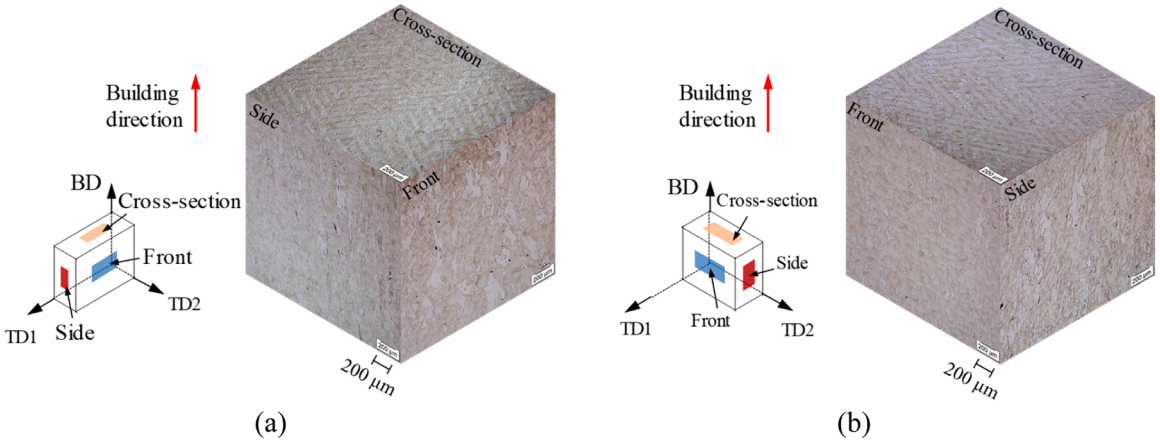


**Fig. 10.** 3D OM microstructure reconstruction of samples extracted from PBF (a) 316L-3 and (b) 316L-4 coupons, both showing the laser tracks along the build direction and the scanning pattern.

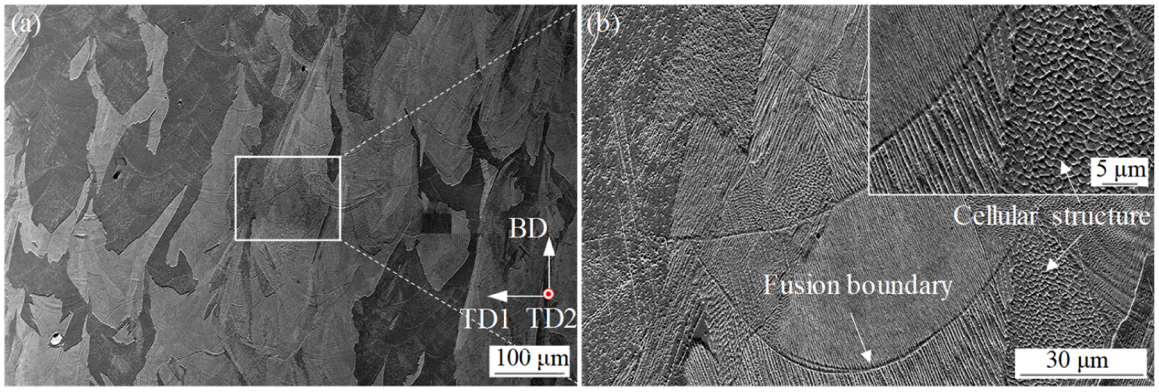


**Fig. 11.** SEM micrographs in the TD1-BD plane (side view of the sample from 316L-4 coupon): (a) microstructure at different length scales and (b) high magnification SEM images, showing the fusion boundaries, columnar grains and cellular structure.

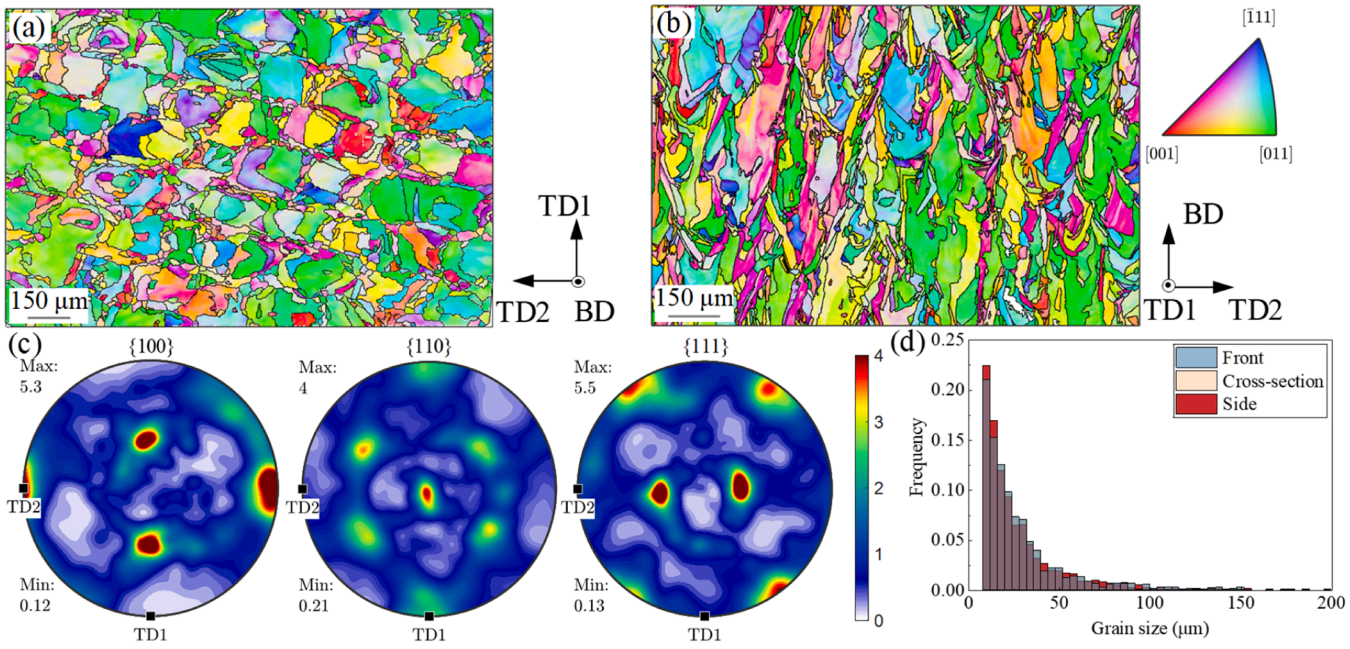


**Fig. 12.** Inverse pole figure (IPF) maps of the L-PBF 316L (a) cross-section and (b) front samples, with IPF maps coloured with respect to the build direction (IPF-BD), (c) pole figures of cross-section sample and (d) grain size distribution of three samples. Samples extracted from the 316L-4 coupon.

crystal cells (or dendrites) can be seen within the melt pools, growing epitaxially across multiple melt pools (see Fig. 11(b)).

Inverse pole figures (IPF) enable the visualisation of local crystal directions using a colour-coding scheme, while pole figures provide insight into the texture, where each point on the pole figure corresponds to the orientation of a specific crystallographic plane or direction relative to the reference frame of the sample. Fig. 12 presents (a, b) the IPF maps with overlaid grain boundaries with respect to the build direction (IPF-BD) of the cross-section and front samples, (c) the {100}, {110} and {111} pole figures of the cross-section sample, and (d) the grain size distribution of three samples extracted from the 316L-4 coupon. The contour levels of orientations in the pole figures show the strength of the texture as a multiple of random occurrence. The IPF maps show that columnar grains, oriented mainly in the ⟨100⟩ and ⟨110⟩ directions, featured most prominently in the build direction. The preferred crystallographic orientations were further confirmed by the pole figures of the TD1-TD2 plane, as shown in Fig. 12(c), where high concentrations of the {100} plane normals along the TD2 and the {110} plane normals along the TD1 and BD were found, indicating a strong ⟨100⟩ and ⟨110⟩ crystallographic texture. The ⟨100⟩ and ⟨110⟩ texture seen in L-PBF 316L stainless steel was attributed in [50,51] to the occurrence of the epitaxial grain growth, with ⟨100⟩ being the preferred crystallographic orientation for grain growth in FCC materials, and side-branching, respectively. The grain size, which is defined as the diameter of a circle with an equivalent area to that of the grain, was measured using EBSD in accordance with ASTM: E2627-23 [52]. The average grain sizes in the scanned areas of the front, cross-section and side samples were measured to be 28.0 μm, 24.2 μm and 29.1 μm, respectively.

As discussed above, L-PBF 316L stainless steel exhibits a multi-scale microstructure consisting of melt pools, columnar grains and an intragranular cellular network, whereas wrought 316L stainless steel consists only of micron-scale grains [15]. A significantly increased yield strength in the printed 316L stainless steel relative to its wrought counterparts has been reported in many studies [15,37–39], while the source of strengthening is not, as yet, fully understood. Some researchers emphasized the effect of solidification sub-grains (i.e. cells) and predicted the yield strength using the cell size in the modified Hall-Petch equation [36], while others referred to the traditional strengthening mechanisms to explain the mechanical properties of the printed material [15,53]. The contribution of cells in the printed material is to enhance the dislocation density, since a large number of dislocations were observed at the cell boundaries and within the cells from transmission electron microscopy (TEM) [15,53]. The average cell size was measured to be 1.5 μm based on a series of high-magnification SEM images (an example of which is shown in Fig. 11(b)). The measured cell size and grain size correspond to a calculated 0.2 % proof strength of 391 N/mm$^2$ according to [36] and of 464 N/mm$^2$ according to [15], respectively, both of which are relatively close to the measured value of 431 N/mm$^2$.

### 4.3. Microstructural characterisation of L-PBF CX stainless steel

The cross-sectional microstructure and particle size distribution of the gas-atomised stainless steel CX powders are shown in Fig. 13. The powder particles were mainly spherical with smooth surfaces, and only a small portion of satellite particles were adhered; the average measured particle size was 35.3 μm, with a range of 20~63 μm (see Fig. 12), in line with the nominal particle size distribution provided by the manufacturer EOS [28].

Fig. 14 shows the SEM micrographs of the side (scanning plane, i.e. TD1-TD2 plane) and cross-section (build plane, i.e. TD1-BD plane) samples of the L-PBF CX stainless steel at different magnifications. The microstructure of the material in the TD1-TD2 plane reveals the scan tracks with a non-uniform arrangement due to the employed scanning strategy (see Fig. 14(a) and (b)). The measured widths of the tracks were approximately 100 μm, which were similar to the laser spot diameter. The observed cross-section sample exhibited a microstructure with overlapped melt pools which were formed due to the successive solidification. The microstructure of the L-PBF CX stainless steel consisted primarily of cellular structures, cellular dendritic grains and martensite packets with nearly parallel laths. A large quantity of dendritic grains, with growth direction indicated by the yellow arrows in Fig. 14(d), were seen to grow parallel to the heat flow direction (indicated by red arrows in Fig. 14(d)), while no secondary dendrite structure was seen in these samples from the SEM results.

Fig. 15 shows the EBSD results, including (a, b) the inverse pole figure (IPF) maps constructed using the IPF-BD colouring and grain boundary maps of the side and cross-section samples, (c) the {100}, {110} and {111} pole figures of the side sample and (d) the grain size distribution of the front, side and cross-section samples. The phase structure of stainless steels can be predicted based on the chromium and nickel equivalent values ($Cr_{eq}$, $Ni_{eq}$) according to the Schaeffler-DeLong diagram [54]; for the examined CX stainless steel, martensite and austenite phases were expected. The fractions of the austenite and martensite phases were measured to be approximately 2 % and 98 %, respectively, through EBSD analysis. The primary martensite phase in the L-PBF samples, is mainly attributed to the low nickel content in CX stainless steel, which improves the stability of martensite and inhibits the formation of reverted austenite after the rapid cooling processes [42,43]. The IPF maps of the two samples show the existence of columnar and equiaxed grains, while the pole figures show a weak ⟨111⟩ texture (parallel to BD) with a maximum intensity of about 3.0 times the random intensity, which is consistent with previous studies [43–45] but, overall,

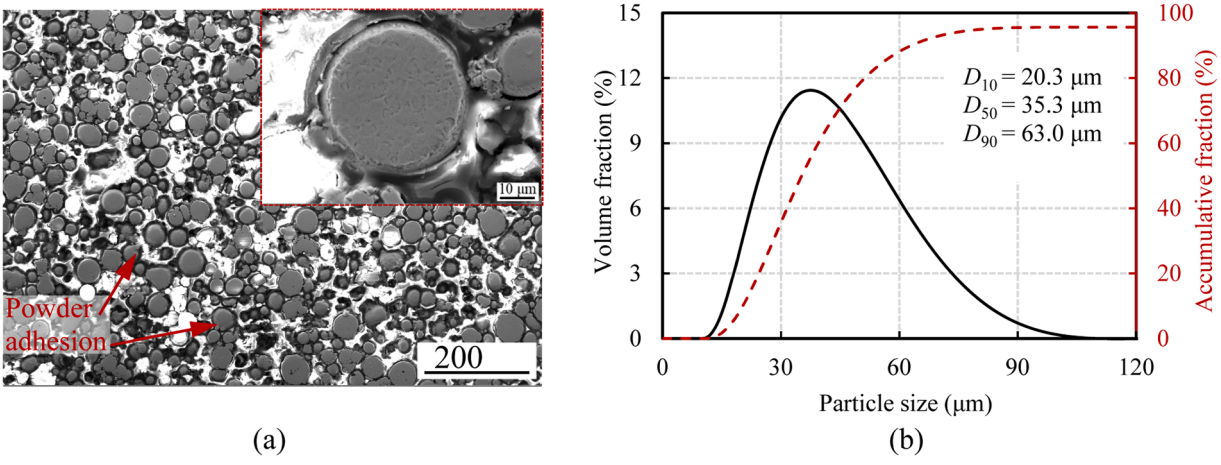


**Fig. 13.** (a) SEM image of the cross-sections and (b) particle size distribution of CX stainless steel powder.

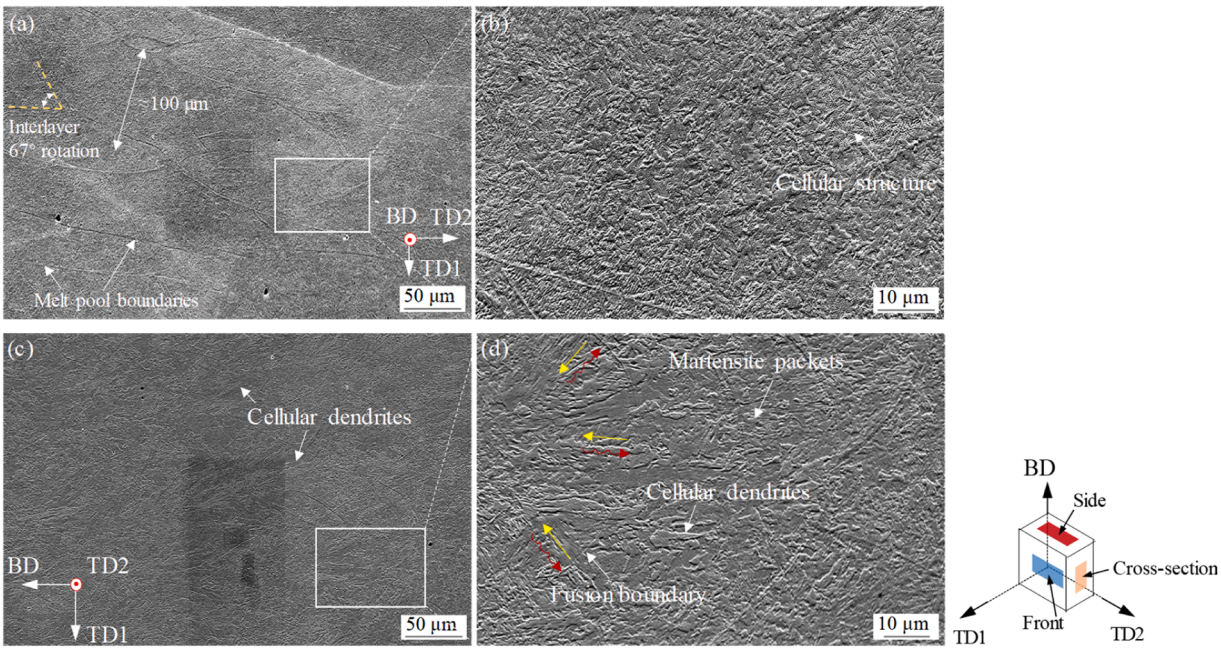


**Fig. 14.** SEM micrographs of the L-PBF CX stainless steel (a, b) side and (c, d) cross-section samples.

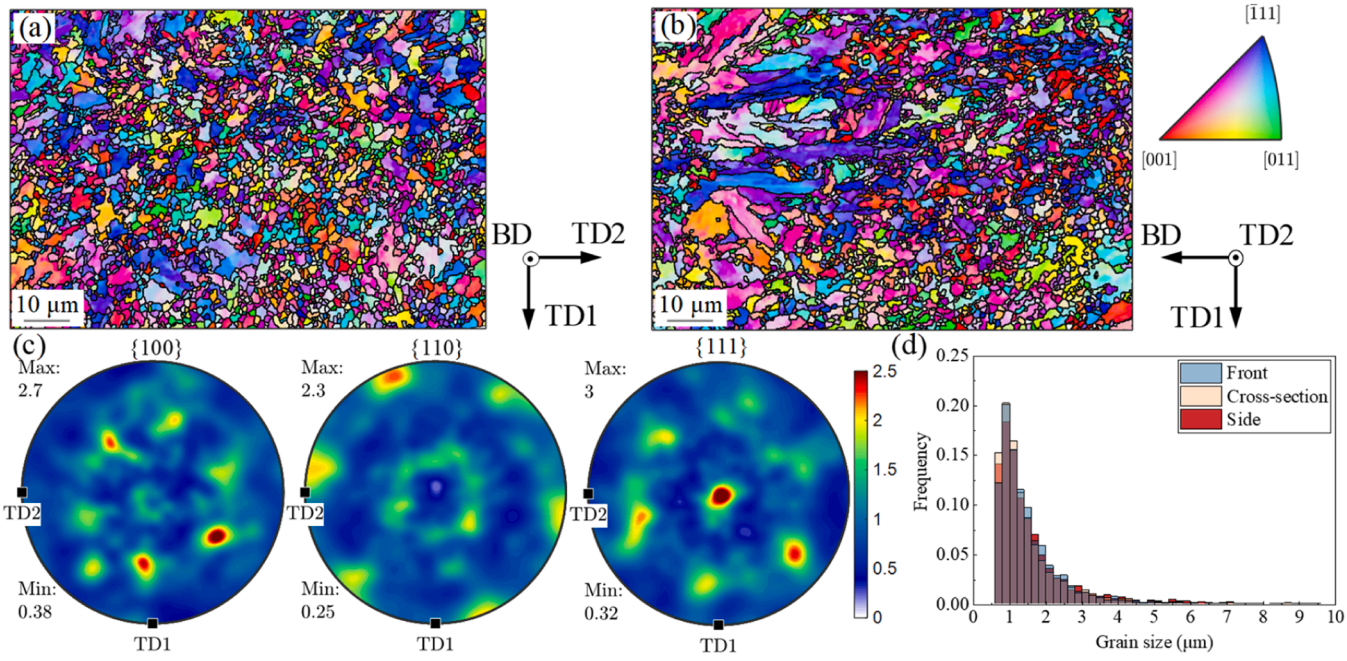


**Fig. 15.** Inverse pole figure (IPF) maps of the L-PBF CX stainless steel (a) side and (b) cross-section samples, with IPF maps coloured with respect to the build direction (IPF-BD), (c) pole figures of side sample and (d) grain size distribution of three samples. Samples extracted from the CX-3 coupon.

the grains have no strong crystallographic orientation. Fig. 15(d) shows that there was no significant difference in the grain size distribution range for the three samples. The average grain sizes of the front, cross-section and side samples of the L-PBF CX stainless steel were 1.62 μm, 1.50 μm and 1.43 μm, respectively, and 97 % of the observed grains were smaller than 5 μm. The formation of such fine grains can be attributed to the rapid solidification [6].

## 5. Geometric measurements

The cylindrical shell test specimens had a nominal outer diameter $D\times$ thickness $t$ (in mm) of C150 × 1.0, C180 × 1.0, C200 × 1.0, C150 × 0.7, C180 × 0.7 and C200 × 0.7, covering a range of cross-sectional slenderness values. The nominal specimen lengths $L$ were set equal to the outer diameters of the shells, which were greater than twice the axisymmetric meridional elastic buckling half-wavelengths and have been adopted in several previous studies on shell buckling [21,55]. Prior to end potting, the geometric properties of each specimen were obtained through calliper and Archimedes' measurements, along with 3D-laser scanning, as shown in Fig. 16(a). Measurements of the outer diameter $D$ and wall thickness $t$ at both ends of the shells, as well as the overall specimen length $L$, were taken at 30° intervals around the perimeter of the specimens using a digital calliper. The volume $V$ of each specimen was determined based on Archimedes' method, and the average

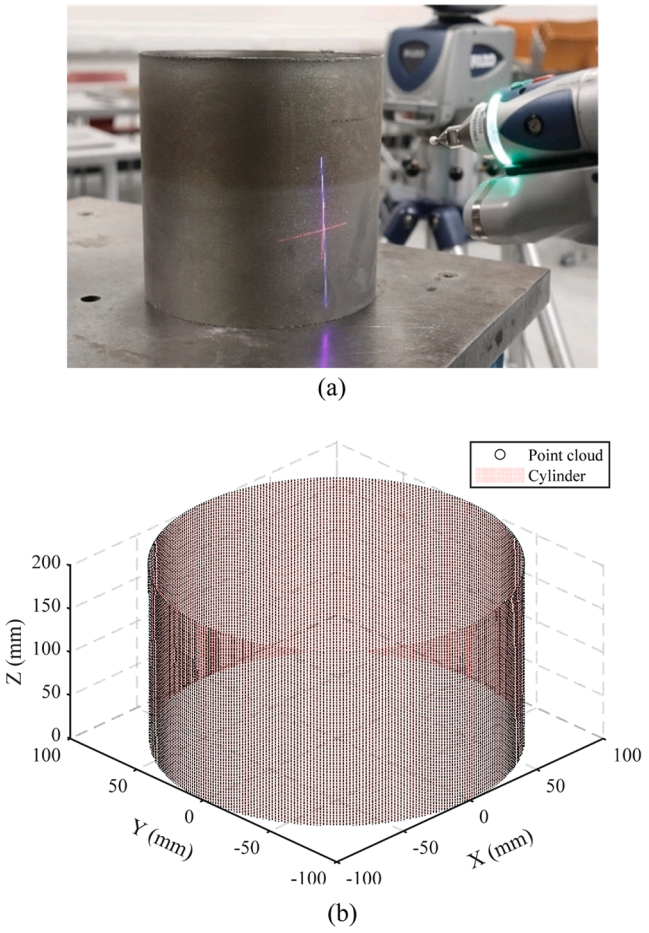


**Fig. 16.** (a) Setup for geometric measurements using 3D-laser scanning and (b) visualisation of point cloud data of a cylinder.

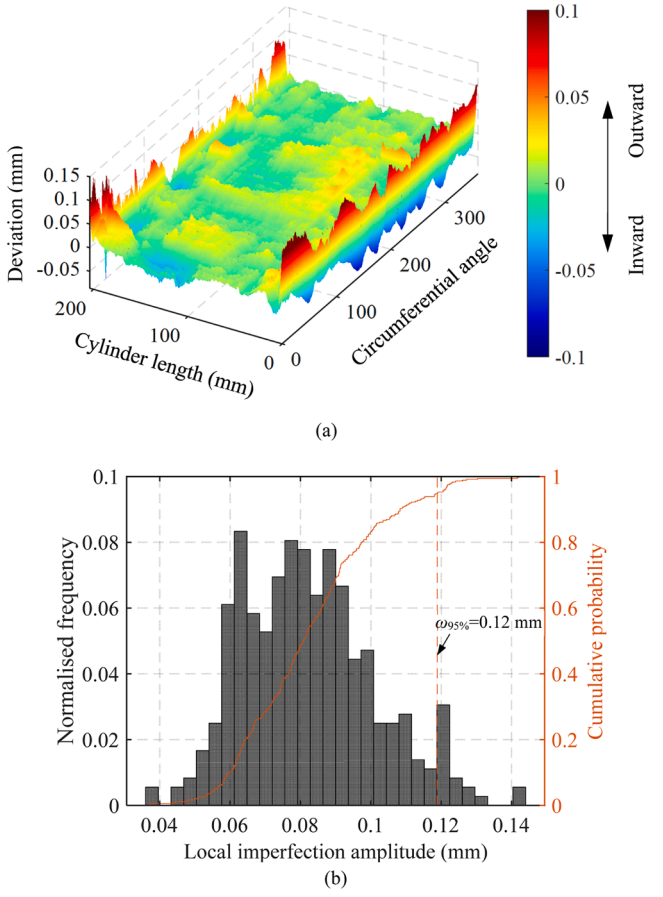


**Fig. 17.** (a) Typical measured imperfection distribution of test shell—unwound plot and (b) histogram and CDFs of longitudinal imperfections in the shell specimen C200 × 0.7.

cross-sectional area $A$ was calculated by dividing the volume $V$ by the average length $L$. All examined specimens were medium-length cylinders according to EN 1993-1-6 [56]. To provide accurate and detailed out-of-straightness characteristics of each specimen, a non-contact laser scanner (FARO Design ScanArm 2.0), with a reported accuracy of ±0.075 mm and a minimum point spacing of 40 μm within its measurement range of 2.5 m [57], was utilised to scan the external and internal surfaces.

The point cloud data were pre-processed in Geomagic Wrap [58], including deletion of unwanted data, hole filling, model alignment and merging. The overall scan volume was verified against the volume measurements based on Archimedes' principle. The processed data were imported into Rhino [59] in the form of polygon meshes, which were contoured into cross-section slices along the specimen length and then vertically sectioned into sets of longitudinal points at 1° intervals around the circumference of the shells. The deviations from a linear trend line fitted to each set of longitudinal points were taken as the local geometric imperfections; a similar approach to the determination of longitudinal imperfections using scan data was reported in [4]. A typical imperfection distribution processed from the scan data of the specimen C200 × 0.7 is shown in Fig. 17, where outward and inward deviations are denoted as positive and negative, respectively. The local imperfection amplitude of each specimen $\omega_{max}$ was defined as the maximum absolute deviation over the entire specimen. The measured imperfection amplitudes satisfied the EN 1993-1-6 [56] Class A fabrication quality requirements for all test specimens except C150 × 1.0 (which slightly exceeded the Class A limits). The limiting Class A characteristic imperfection amplitude $\Delta\omega_k$ was calculated as:

$$\Delta\omega_k = \frac{1}{Q}\sqrt{rt} \tag{1}$$

where $Q$ is the fabrication quality parameter, taken as 40 for Class A.

A probabilistic treatment of the longitudinal imperfection amplitudes around the circumference of each specimen has also been performed to examine the variation in the imperfection data. A histogram constructed from the 360 local imperfection amplitude measurements (at intervals of 1°) is plotted for a typical shell specimen (C200 × 0.7) in Fig. 17, along with the corresponding empirical cumulative distribution function (CDF) curve. A CDF value, denoted as $P(\boldsymbol{\Delta} < \omega_p)$, represents the probability that a randomly selected imperfection amplitude $\boldsymbol{\Delta}$ is less than a particular imperfection amplitude value $\omega_p$ [60,61]; the characteristic imperfection amplitude $\omega_{95\,\%}$ with a CDF value of 95 % for each specimen is presented in Table 6.

## 6. Compression testing

Six axial compression tests were performed on the L-PBF stainless steel circular cylindrical shells to investigate their cross-sectional response and load-bearing capacity. Five of the specimens were manufactured from 316L stainless steel, while one was manufactured from CX stainless steel; testing of the latter specimen was previously reported in [19], thus only the key test outputs are presented herein. The printed (top) end of each specimen was finished to a high degree of geometric accuracy, while the lower end that had been sawn off from the build plate had to be machined flat and square such that a uniform stress distribution over the cross-section could be maintained during testing.

**Table 6**
Measured geometric properties of the test shells and key test results.

| Specimen | Material | $D$ (mm) | $t$ (mm) | $L$ (mm) | $V_{Arch}$ (mm$^3$) | $V_{laser}$ (mm$^3$) | $A_{Arch}$ (mm$^2$) | $\omega_{max}$ (mm) | $Q$ | $\omega_{95\%}$ (mm) | $D/t\varepsilon^2$ | $\bar{\lambda}_c$ | $L/\sqrt{rt}$ | $m$ | $N_u$ (kN) | $\delta_u$ (mm) | $N_u/\sigma_{0.2}A$ |
|---|---|---|---|---|---|---|---|---|---|---|---|---|---|---|---|---|---|
| C150 × 1.0 | 316L | 149.6 | 1.02 | 159.6 | 76520 | 76042 | 479.3 | 0.23 | B | 0.20 | 341.5 | 0.56 | 18.4 | 5 | 186.8 | 0.62 | 0.90 |
| C180 × 1.0 | 316L | 179.5 | 1.04 | 189.8 | 109458 | 111121 | 576.8 | 0.23 | A | 0.21 | 400.0 | 0.61 | 19.7 | 6 | 208.2 | 0.59 | 0.83 |
| C200 × 1.0 | CX | 200.1 | 1.02 | 152.7 | 93773 | 95542 | 614.1 | 0.19 | A | 0.15 | 759.3 | 0.84 | 15.2 | 7 | 366.4 | 0.57 | 0.76 |
| C150 × 0.7 | 316L | 149.6 | 0.75 | 159.8 | 55209 | 56126 | 345.4 | 0.17 | A | 0.16 | 463.4 | 0.65 | 21.4 | 7 | 113.3 | 0.50 | 0.75 |
| C180 × 0.7 | 316L | 179.5 | 0.74 | 189.8 | 78114 | 79036 | 411.7 | 0.14 | A | 0.13 | 562.8 | 0.72 | 23.3 | 8 | 125.7 | 0.49 | 0.70 |
| C200 × 0.7 | 316L | 199.5 | 0.74 | 209.0 | 96349 | 97260 | 461.1 | 0.14 | A | 0.12 | 623.7 | 0.76 | 24.3 | 9 | 130.2 | 0.49 | 0.65 |

Special care was taken during the end machining—wooden blocks were precisely made and inserted into the thin-walled cylinders to reinforce the clamped regions. The top and bottom cylinder edges of each specimen were then bonded to outer and inner metallic ring stiffeners of 10 mm thicknesses using Araldite 2011 reinforced epoxy adhesive to avoid premature end failure and to ensure fixed boundary conditions.

All the compression tests were conducted using an Instron 3500 kN hydraulic testing machine; the test setup is presented in Fig. 18. The instrumentation for the compression tests consisted of three potentiometers positioned at 120° intervals, coupled with three equally spaced strain gauges affixed to each specimen at mid-height to measure the axial deformations, and a load cell within the testing machine to record the applied load. A four-camera LaVision DIC system was employed to measure the surface deformations of the specimens from two sides at 90° to each other by tracking the movement of black and white speckle patterns that were applied to the specimen surfaces prior to testing. A self-locking ball seating was positioned between the crosshead of the testing machine and the top end platen to accommodate any possible out-of-squareness and to ensure uniform axial loading. Hardened end platens were placed at both ends of the specimens to avoid damage to the testing machine from the high level of the localised stresses. The tests were performed under displacement control, with a compressive strain rate of approximately 0.1 % min$^{-1}$, and were continued beyond the ultimate load to observe the initial unloading behaviour. The axial load, top platen movement, potentiometer and strain gauge readings and DIC images, were recorded at 1-second intervals.

The post-ultimate out-of-plane deformations of all test specimens are shown in Fig. 19 to aid visualisation of the failure modes, where outward and inward deformations are denoted as positive (coloured in red) and negative (coloured in blue), respectively. All circular cylindrical shells failed by local buckling in an asymmetric 'chequerboard' pattern with one longitudinal wave and 5 to 9 circumferential waves, where the number of circumferential waves $m$ for each shell is reported in Table 6. Also reported are the key test parameters and outputs – the local cross-sectional slenderness parameter $D/t\varepsilon^2$, where

$$\varepsilon^2 = \frac{235}{\sigma_{0.2}} \frac{E}{210000} \tag{2}$$

is a material parameter, and the normalised cross-sectional slenderness $\bar{\lambda}_c = \sqrt{\sigma_{0.2}/\sigma_{cr}}$, where

$$\sigma_{cr} = \frac{E}{\sqrt{3(1-\nu^2)}} \frac{2t}{D} \tag{3}$$

is the elastic local buckling stress, the length parameter $L/\sqrt{Rt}$, the peak load $N_u$, the end shortening at the peak load $\delta_u$ and the ratio of the peak load $N_u$ to the yield load $\sigma_{0.2}A$.

The axial load-end shortening curve and DIC results for a typical stub column test specimen—C180 × 0.7—are presented in Fig. 20, where the axial strain distributions and failure mode can be clearly seen. All axial load-end shortening curves obtained from (i) the potentiometer and strain gauge readings, with the elastic deformations of the end platens eliminated [62], and (ii) the DIC data, by summing longitudinal differential deformations along the specimen length, are plotted in Fig. 21. The two approaches to the calculation of end shortening are shown to yield essentially identical results. All test specimens exhibited sharp unloading behaviour, which is a characteristic of shells and other structural systems [63,64] that possess an unstable post-buckling response. The shells failed below the yield load $\sigma_{0.2}A$ and the test results revealed the anticipated trend of lower capacities relative to the yield load with increasing local slenderness, reflecting the increased susceptibility to local buckling. Note that all shell test specimens were printed in the $\theta = 90°$ direction; although the material strengths were found to be lowest in this direction, this remains the most practical

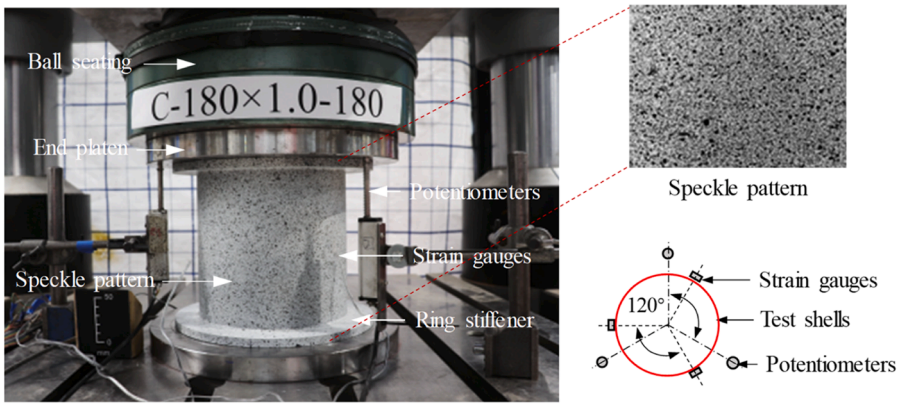


**Fig. 18.** Experimental configuration for shell compression tests.

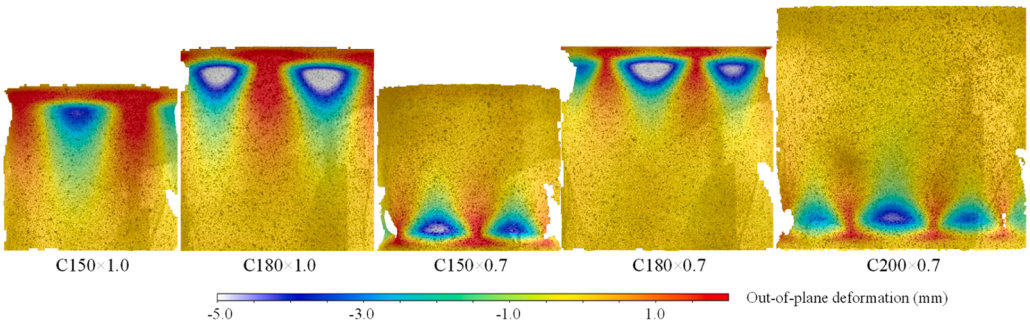


**Fig. 19.** Post-ultimate out-of-plane deformations (unit: mm) of cylindrical shells, with increasing slenderness from left to right.

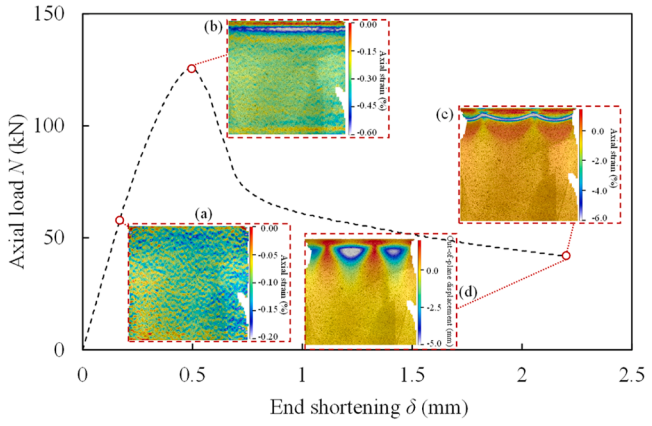


**Fig. 20.** Typical axial load end-shortening curve and DIC results from the compression test on specimen C180 × 0.7, showing axial strain distributions (unit: %) (a) at $0.5N_u$, (b) just after $N_u$ and (c) when unloading (also showing (d) out-of-plane deformations).

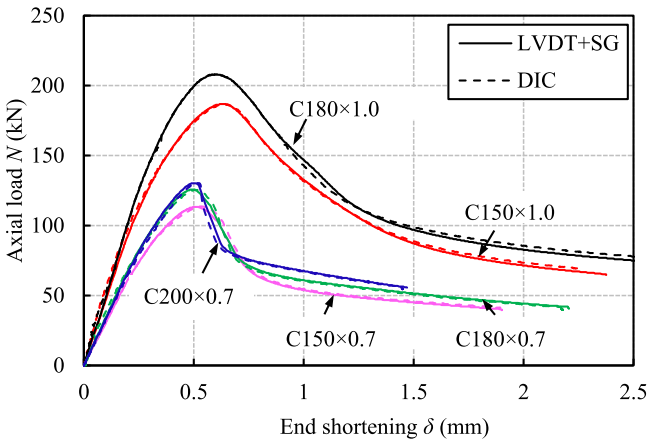


**Fig. 21.** Measured axial load end-shortening curves of all test specimens.

printing strategy.

## 7. Comparisons with existing design provisions

### 7.1. General

The European stability design provisions for cylindrical steel shells are set out in EN 1993-1-6 [56], which utilises the concept of fabrication tolerance quality classes to reflect the sensitivity of the buckling resistance of shells to local imperfections. The applicability of these provisions to additively manufactured cylindrical shells is assessed herein through comparisons against the generated experimental data, as well as additional results established numerically. Comparisons are also made against existing test data on conventionally manufactured cylindrical shells. In the comparisons presented, the measured (or modelled) material and geometric properties of the test (or FE) specimens are employed, and all partial safety factors for resistance are taken to be unity. A total of 683 experimental and 3096 numerical data points pertaining to axially compressed cylindrical shells are considered in this work.

### 7.2. Assembled test dataset

Experimental data on axially compressed metallic cylindrical shells from 61 previous studies [21–23,65–122] have been collected. Only specimens with lengths satisfying $1 < L/L_c < 100$ and $L/R < 10$ were considered, where $L_c$ is the classical meridional half-wavelength, calculated as $L_c = \frac{\pi}{[12(1-\upsilon^2)]^{1/4}}\sqrt{rt}$, where $\upsilon$ is the Poisson's ratio, $r$ is the radius of the cylinder and $t$ is the thickness, to ensure the shells were sufficiently long to prevent end effects and to contain a representative pattern of local imperfections but still short enough to preclude global buckling. The full dataset contained 679 specimens, consisting of 371 on steel [21–23,65–99], 172 on aluminium [96,97,100–113], 51 on brass [94,95,98,99,109,114,115], 45 on copper [116–118] and 40 on nickel [55,98,119–122] shells. The collected results, together with the L-PBF stainless steel stub column data from the present study and from [4], are analysed in Section 7.5.

### 7.3. Complementary numerical data

Two computational analyses—a linear bifurcation analysis (LBA) and a geometrically and materially nonlinear analysis (GMNIA), were conducted using the software package Abaqus 2022 [123] to expand the database of axially compressed L-PBF stainless steel cylinders. LBA was used to generate an eigenmode geometry to represent the local imperfection pattern, and a measured (or modelled) imperfection amplitude was used to scale the pattern in a subsequent GMNIA, as recommended in EN 1993-1-6 [56]. The four noded shell element with reduced integration (S4R) from the ABAQUS element library [123], which has been successfully used in previous studies on thin-walled stainless steel structural elements [124–128], was employed with 5 integration points through the thickness. The employed mesh size was set equal to 0.2 $(Dt)^{1/2}$, which is approximately 15 % of the theoretical axisymmetric elastic bucking half-wavelength in compression, as recommended by Zhang et al. [19]; this mesh size was found to be sufficiently fine for capturing the local buckling behaviour of the cylindrical shells while maintaining high computation efficiency. Fixed boundary conditions, as employed in the tests, were simulated by coupling the end sections of the cylinders to reference points, with all degrees of freedom, except longitudinal displacement at the top reference point, restrained, as shown in Fig. 22. For both the FE validation and parametric studies, the adopted material stress-strain curves for the L-PBF 316L and CX stainless

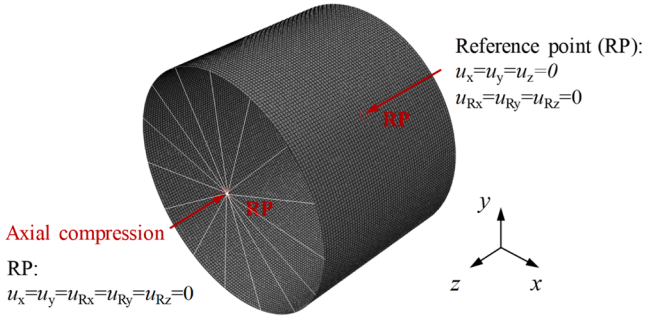


**Fig. 22.** Geometry, loading and boundary conditions of FE models for cylinders.

steels were derived by averaging the two-stage Ramberg-Osgood parameters from the tensile tests, as summarised in Tables 3 and 4.

The established FE models were validated against the experimental results, considering failure modes (see Fig. 23, where outward and inward deformations are coloured in red and blue, respectively) for all cylindrical shells and typical load-deformation histories (Fig. 24). The ratios of the numerical to experimental peak loads $N_{u,FE}/N_{u,test}$ and corresponding deformations $\delta_{u,FE}/\delta_{u,test}$ for all shell specimens, together with the test and FE number of circumferential waves, are reported in Table 7. The numerical failure modes, number of circumferential waves, peak loads and deformations at the peak loads generally match the experimental results, indicating the successful replication of the buckling behaviour of thin cylindrical shells manufactured by L-PBF.

Upon validation of the developed FE models, parametric studies were performed considering a wide range of cross-sectional slenderness values $\bar{\lambda}_c$, the (from 0.2 to 2.0) and length-to-radius ratios (from 1.5 to 2.5), two different stainless steel grades (CX and 316L) and four levels of imperfection amplitudes (corresponding to fabrication tolerance quality Classes A, B and C in EN 1993-1-6 [56] and worse than Class C ($Q = 10$)). In total, 3096 axial compressive resistance results were generated in the numerical simulations.

### 7.4. EN 1993-1-6 design provisions

According to the European standard EN 1993-1-6 [56], axially compressed cylindrical shells are divided into short ($L\sqrt{rt} < 1.7$), medium ($1.7 \le L\sqrt{rt} \le 0.5r/t$) and long ($L\sqrt{rt} > 0.5r/t$) length cylinders. A factor $C_x$ is used to scale the elastic critical buckling stress $\sigma_{cl}$ for short and long cylinders, and the modified meridional squash limit is applied for long cylinders. This standard uses a generic capacity curve that correlates the buckling reduction factor $\chi$ (equal to $R_k/R_{pl}$) of a shell with its relative slenderness $\bar{\lambda}_c$ defined as $\sqrt{R_{pl}/R_{cl}}$ from Eq. (4), where $R_k$ represents the characteristic buckling resistance, and $R_{pl}$ and $R_{cl}$ are the reference plastic and elastic critical buckling resistances, respectively.

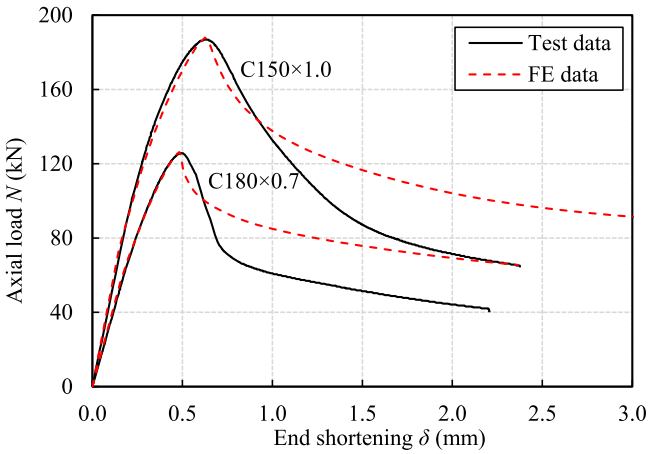


**Fig. 24.** Comparisons of typical experimental and numerical load-deformation curves for 316L cylindrical shells.

$$\chi = \begin{cases} \chi_h - \bar{\lambda}_c/\bar{\lambda}_0(\chi_h - 1) & \text{when } \bar{\lambda}_c \le \bar{\lambda}_0 \\ 1 - \beta\left(\dfrac{\bar{\lambda}_c - \bar{\lambda}_0}{\bar{\lambda}_p - \bar{\lambda}_0}\right)^{\eta} & \text{when } \bar{\lambda}_0 < \bar{\lambda}_c < \bar{\lambda}_p \\ \dfrac{\alpha}{\bar{\lambda}_c^{\,2}} & \text{when } \bar{\lambda}_p \le \bar{\lambda}_c \end{cases} \quad (4)$$

The characteristic buckling resistance $R_k$ can be derived from experiments or the geometrically and materially nonlinear analysis (GMNIA) of an imperfect shell, and the two reference resistances $R_{pl}$ and $R_{cr}$ can be determined from materially nonlinear and linear bifurcation analyses (MNA and LBA), respectively. The capacity curve comprises stocky (plastic collapse), slender (elastic buckling) and intermediate (elastic-plastic buckling) segments, as shown in Fig. 25, and is controlled by key capacity parameters, including the hardening limit $\chi_h$, the squash limit slenderness $\bar{\lambda}_0$, the elastic buckling reduction factor $\alpha$, the plastic range factor $\beta$, the interaction exponent factor $\eta$ and the plastic limit relative slenderness $\bar{\lambda}_p$, as summarised in Table 8 for medium-length cylinders under uniform axial compression. To allow for the effects of geometric imperfections, the parameters $\alpha$, $\beta$ and $\eta$ are defined as a function of the imperfection amplitude $\Delta\omega_k$ (equal to $\frac{1}{Q}\sqrt{rt}$), which is related to the fabrication quality parameter $Q$, where $Q$ is respectively taken as 40, 25 and 16 for Class A (excellent), Class B (high) and Class C (normal). For materials with nonlinear stress-strain curves, such as stainless steels [129], a reduced value of the elastic modulus $E_{red}$, which can be conservatively taken as the secant modulus at the 0.2 % proof stress $E_{sec}$, is used in the determination of the elastic critical stress $\sigma_{cl}$ or load $R_{cl}$ [56]. The collected test data, together with that generated in the present study, are plotted against the cross-sectional slenderness $\bar{\lambda}_c$ in Fig. 26(a), together with the EN 1993-1-6 design curve for L-PBF 316L

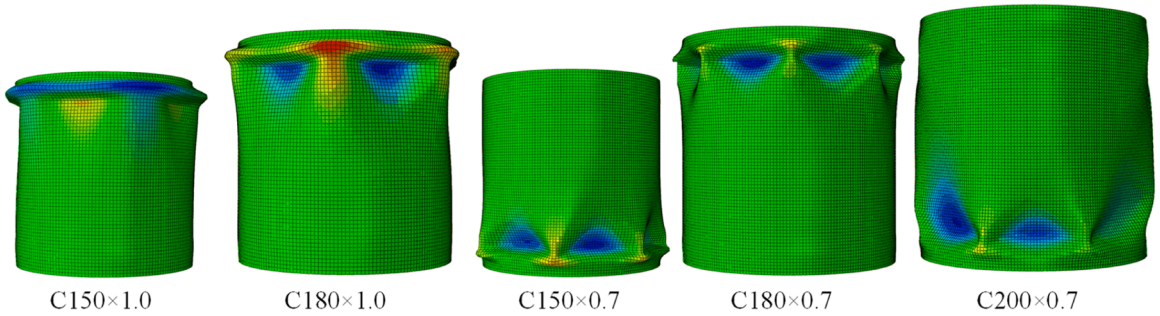


**Fig. 23.** Numerical failure modes of the tested circular cylindrical shells, with increasing slenderness from left to right.

**Table 7**
Comparisons of test results with FE results for test shells.

| Specimen | Material | $N_{u,test}$ (kN) | $\delta_{u,test}$ (mm) | $m_{test}$ | $N_{u,FE}$ (kN) | $\delta_{u,FE}$ (mm) | $m_{FE}$ | $\frac{N_{u,FE}}{N_{u,test}}$ | $\frac{\delta_{u,FE}}{\delta_{u,test}}$ |
|---|---|---|---|---|---|---|---|---|---|
| C150 × 1.0 | 316L | 186.8 | 0.62 | 5 | 187.9 | 0.63 | 5 | 1.01 | 1.01 |
| C180 × 1.0 | 316L | 208.2 | 0.59 | 6 | 209.1 | 0.64 | 6 | 1.00 | 1.08 |
| C200 × 1.0 | CX | 366.4 | 0.57 | 7 | 366.8 | 0.54 | 7 | 1.00 | 0.94 |
| C150 × 0.7 | 316L | 113.3 | 0.50 | 7 | 112.2 | 0.45 | 7 | 0.99 | 0.90 |
| C180 × 0.7 | 316L | 125.7 | 0.49 | 8 | 126.3 | 0.48 | 8 | 1.00 | 0.99 |
| C200 × 0.7 | 316L | 130.2 | 0.49 | 9 | 130.3 | 0.62 | 9 | 1.00 | 1.27 |
| | | | | | | | Mean | 1.00 | 1.03 |
| | | | | | | | COV | 0.01 | 0.13 |

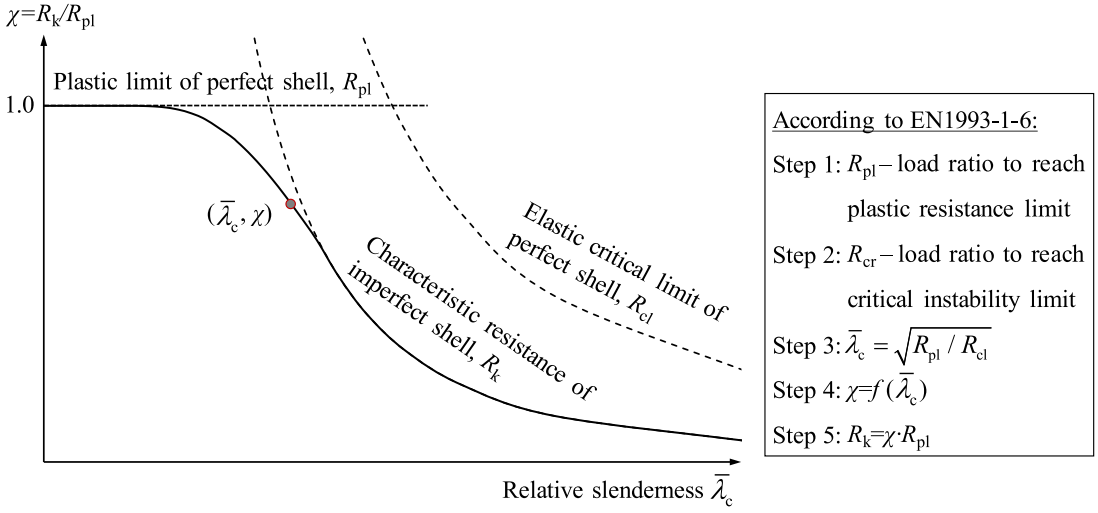


**Fig. 25.** Basic concept and procedure of EN 1993-1-6 buckling design specification.

**Table 8**
Meridional buckling parameters for medium-length cylinders from EN 1993-1-6 [56].

| Elastic buckling reduction factor $\alpha$ | Plastic range factor $\beta$ | Interaction exponent $\eta$ | Hardening limit $\chi_h$ | Squash limit slenderness $\bar{\lambda}_0$ | Plastic limit slenderness $\bar{\lambda}_p$ |
|---|---|---|---|---|---|
| $\frac{0.83}{1+2.2(\Delta\omega_k/t)^{0.88}}$ | $1-\frac{0.95}{1+1.2(\Delta\omega_k/t)}$ | $\frac{5.4}{1+4.6(\Delta\omega_k/t)}$ | 1.0 | 0.2 | $\sqrt{\frac{\alpha}{1-\beta}}$ |

stainless steel cylindrical shells with Class A fabrication quality; the generated FE data for 316L and CX stainless steel cylindrical shells with four levels of imperfection amplitudes are plotted in Fig. 26(b) and (c). EN 1993-1-6 may be seen to provide safe-sided predictions for the buckling resistances of axially compressed cylindrical shells manufactured by L-PBF.

### 7.5. Assessment of resistance predictions

Comparisons between the ultimate loads from the experiments and numerical simulations and the EN 1993-1-6 resistance predictions are made in this sub-section. The normalised compressive resistances $N_u/N_{u,pred}$ are plotted against the cross-sectional slenderness in Fig. 27, and the statistical results are provided in Table 9, where $N_{u,EC3}$ are the resistance predictions derived from EN 1993-1-6 [56] and COV is the coefficient of variation. EN 1993-1-6 may be seen to yield generally consistent and safe-sided predictions of the buckling strength of the tested and modelled L-PBF stainless steel cylindrical shells across a wide range of cross-sectional slendernesses, though with increasing scatter at higher slenderness.

## 8. Conclusions

This paper presents an experimental and numerical study into the buckling behaviour of additively manufactured stainless steel circular cylindrical shells under axial compression. Six cylindrical shells were additively manufactured using L-PBF, and examined from a microstructural, material and cross-sectional perspective. The tested L-PBF 316L stainless steel exhibited some mechanical anisotropy, with the $\theta = 0^\circ$ coupons showing higher strengths but substantially reduced ductility compared to the $\theta = 90^\circ$ coupons. Compression tests were carried out to ascertain the local buckling resistance of the studied shells. The initial geometric imperfections and deformations (and strains) were measured using the state-of-the-art techniques—3D-laser scanning and digital image correlation. All cylindrical shells buckled below their yield loads in an asymmetric chequerboard pattern and showed the anticipated

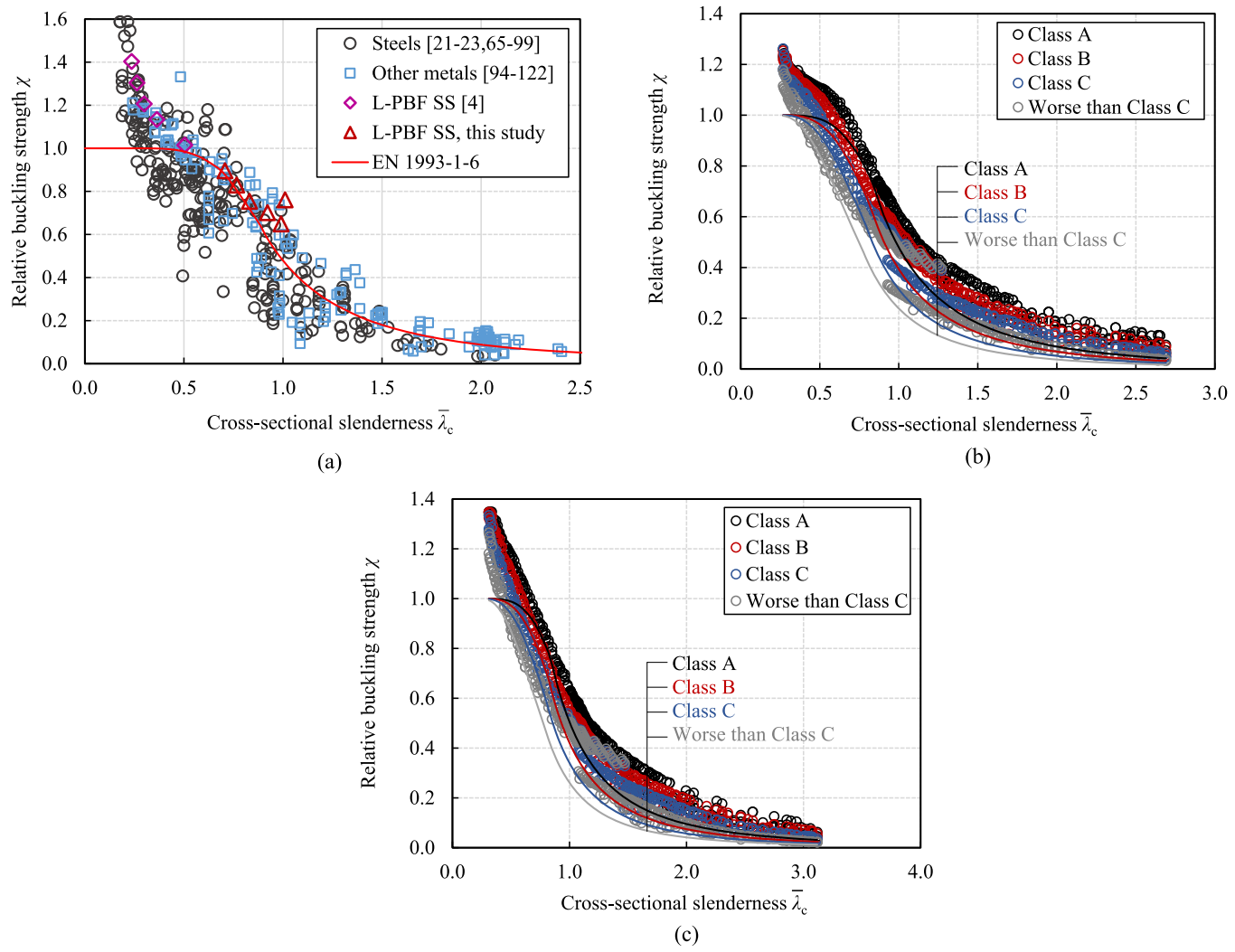


**Fig. 26.** Comparisons of (a) experimental and numerical buckling resistance with EN 1993-1-6 resistance predictions for L-PBF (b) 316L and (c) CX stainless steel CHS in compression, where the design curve in Fig. 26(a) corresponds to the Class A fabrication quality for L-PBF 316L stainless steel.

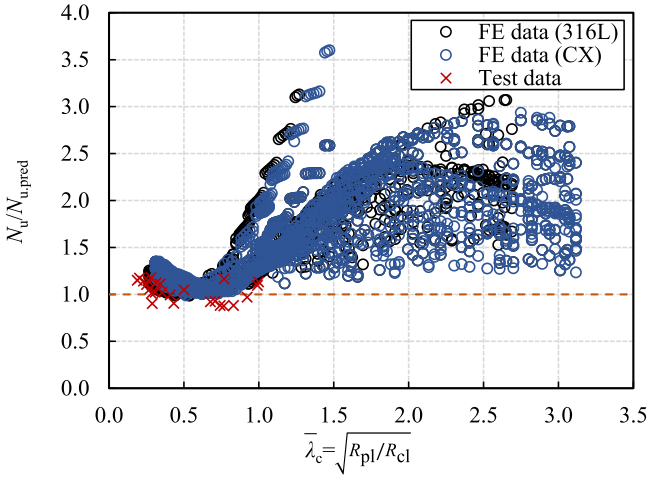


**Fig. 27.** Comparisons of test and FE resistances with resistance predictions from EN 1993-1-6 [56] for circular hollow sections in compression.

**Table 9**
Comparisons of experimental and numerical results with EN 1993-1-6 resistance predictions for stainless steel CHS manufactured by L-PBF.

| Evaluation parameter | Test data, this study | | FE data | |
|---|---|---|---|---|
| | No. of data | $N_u/N_{u,EC3}$ | No. of data | $N_u/N_{u,EC3}$ |
| Mean | 6 | 1.07 | 3096 | 1.63 |
| COV | | 0.08 | | 0.30 |

trend of reducing load-bearing capacity with increasing local slenderness, reflecting the increasing susceptibility to local buckling. The generated experimental and numerical data on L-PBF stainless steel cylindrical shells were used to assess the applicability of EN 1993-1-6; EN 1993-1-6 was found to provide consistent and safe-sided buckling resistance predictions for the studied L-PBF stainless steel cylindrical shells subjected to axial compression, with the Class A fabrication quality being most suitable based on the experimental measurements. The tested cylindrical shells had $D/t$ ratios up to 270; future research could be dedicated to larger and more slender PBF shells as this manufacturing technology advances.

## CRediT authorship contribution statement

**Ruizhi Zhang:** Writing – original draft, Visualization, Validation, Software, Methodology, Investigation, Formal analysis, Data curation. **Mohsen Amraei:** Resources, Methodology, Investigation. **Heidi Piili:** Resources, Funding acquisition. **Leroy Gardner:** Writing – review & editing, Supervision, Project administration, Methodology, Conceptualization.

## Declaration of competing interest

The authors declare that they have no known competing financial interests or personal relationships that could have appeared to influence the work reported in this paper.

## Acknowledgements

The authors would like to acknowledge the contribution of the LUT Laser Materials Processing Laboratory for supplying the test specimens. The assistance from Gordon Herbert, Paul Crudge and Alfredo Olivo during the experiments is also gratefully appreciated.

## Data availability

Data will be made available on request.

## References

[1] L. Gardner, Metal additive manufacturing in structural engineering—review, advances, opportunities and outlook, Structures 47 (2023) 2178–2193.
[2] J. Ye, P. Kyvelou, F. Gilardi, H. Lu, M. Gilbert, L. Gardner, An end-to-end framework for the additive manufacture of optimized tubular structures, IEEE Access. 9 (2021) 165476–165489.
[3] P. Kyvelou, H. Slack, D.D. Mountanou, M.A. Wadee, T.B. Britton, C. Buchanan, L. Gardner, Mechanical and microstructural testing of wire and arc additively manufactured sheet material, Mater. Des. 192 (2020) 108675.
[4] R. Zhang, L. Gardner, C. Buchanan, V.P. Matilainen, H. Piili, A. Salminen, Testing and analysis of additively manufactured stainless steel CHS in compression, Thin-Walled Struct. 159 (2021) 107270.
[5] I.H. Shah, N. Hadjipantelis, L. Walter, R.J. Myers, L. Gardner, Environmental life cycle assessment of wire arc additively manufactured steel structural components, J. Clean. Prod. 389 (2023) 136071.
[6] R. Zhang, C. Buchanan, V.P. Matilainen, D. Daskalaki-Mountanou, T.B. Britton, H. Piili, A. Salminen, L. Gardner, Mechanical properties and microstructure of additively manufactured stainless steel with laser welded joints, Mater. Des. 208 (2021) 109921.
[7] CEN (European Committee for Standardization) (2017). Additive manufacturing—general principles—terminology. EN ISO 52900:2017, Brussels.
[8] L. Gardner, Stability and design of stainless steel structures—review and outlook, Thin-Walled Struct. 141 (2019) 208–216.
[9] X. Yan, C. Chen, C. Chang, D. Dong, R. Zhao, R. Jenkins, J. Wang, Z. Ren, M. Liu, H. Liao, R. Lupoi, S. Yin, Study of the microstructure and mechanical performance of CX stainless steel processed by selective laser melting (SLM), Mater. Sci. Eng. 781 (2020) 139227.
[10] O Zhao, L. Gardner, B. Young, Behaviour and design of stainless steel SHS and RHS beam-columns, Thin-Walled Struct. 106 (2016) 330–345.
[11] Y. Liang, O. Zhao, Y.L. Long, L. Gardner, Stainless steel channel sections under combined loading—Part 1: experimental study and numerical modelling, J. Constr. Steel Res. 152 (2019) 154–161.
[12] M. Kucukler, Z. Xing, L. Gardner, Behaviour and design of stainless steel I-section columns in fire, J. Constr. Steel Res. 165 (2020) 105890.
[13] N. Saliba, E. Real, L. Gardner, Shear design recommendations for stainless steel plate girders, Eng. Struct. 59 (2014) 220–228.
[14] M. Bock, L. Gardner, E. Real, Material and local buckling response of ferritic stainless steel sections, Thin-Walled Struct. 89 (2015) 131–141.
[15] S. Bahl, S. Mishra, K.U. Yazar, I.R. Kola, K. Chatterjee, S. Suwas, Non-equilibrium microstructure, crystallographic texture and morphological texture synergistically result in unusual mechanical properties of 3D printed 316L stainless steel, Addit. Manuf. 28 (2019) 65–77.
[16] D. Karlsson, C.Y. Chou, N.H. Pettersson, T. Helander, P. Harlin, M. Sahlberg, G. Lindwall, J. Odqvist, J. Ulf, Additive manufacturing of the ferritic stainless steel SS441, Addit. Manuf. 36 (2020) 101580.
[17] F. Hengsbach, P. Koppa, K. Duschik, M.J. Holzweissig, M. Burns, J. Nellesen, W. Tillmann, T. Tröster, K.P. Hoyer, M. Schaper, Duplex stainless steel fabricated by selective laser melting-microstructural and mechanical properties, Mater. Des. 133 (2017) 136–142.
[18] T.M. Mower, M.J. Long, Mechanical behavior of additive manufactured, powder-bed laser-fused materials, Mater. Sci. Eng. 651 (2016) 198–213.
[19] R. Zhang, L. Gardner, M. Amraei, C. Buchanan, H. Piili, Testing and analysis of additively manufactured stainless steel corrugated cylindrical shells in compression, J. Eng. Mech. 149 (4) (2023) 04023013.
[20] J.J. Yan, M.T. Chen, W.M. Quach, M. Yan, B. Young, Mechanical properties and cross-sectional behavior of additively manufactured high strength steel tubular sections, Thin-Walled Struct. 144 (2019) 106158.
[21] Seide, P., Weingarten, V.I., & Morgan, E.J. (1960). The development of design criteria for elastic stability of thin shell structures. Final Report: STL/TR-60-0000-19425, Space Technology Laboratories, Inc., Los Angeles, CA. –50.
[22] W.M. Wilson, N.M. Newmark, Strength of Thin Cylindrical Shells as Columns: A Report of an Investigation, University of Illinois, Engineering Experiment Station, 1933. Bulletin No. 255.
[23] W.M. Wilson, Tests of Steel Columns Thin Cylindrical Shells Laced Channels Angles: A Report of Tests, University of Illinois, Engineering Experiment Station, 1937. Bulletin No. 292.
[24] A.I. Celik, O. Zeybek, Y.O. Ozkilic, Effect of the initial imperfection on the response of the stainless steel shell structures, Steel Compos. Struct. 50 (6) (2024) 705–720.
[25] O. Zeybek, A.İ. Celik, Y.O. Ozkilic, Buckling of axially loaded shell structures made of stainless steel, Steel Compos. Struct. 48 (6) (2023) 681.
[26] CEN (European Committee for Standardization) (2015). Eurocode 3 - Design of steel structures, Part 1-4: General rules – Supplementary rules for stainless steels. EN 1993C-4:2006+A1:2015, Brussels, Belgium.
[27] EOS GmbH - Electro Optical Systems. (2017). EOS Stainless Steel 316L Material Data Sheet.
[28] EOS GmbH - Electro Optical Systems (2019). EOS Stainless Steel CX Material Data Sheet.
[29] CEN (European Committee for Standardization). (2016). Metallic materials - Tensile testing - Part 1: Method of test at room temperature. EN ISO *6892-1: 2016*, Brussels, Belgium.
[30] LaVision, Davis 10(2) (2021).
[31] Ramberg, W., & Osgood, W.R. (1943). Description of stress-strain curves by three parameters.
[32] E. Mirambell, E. Real, On the calculation of deflections in structural stainless steel beams: an experimental and numerical investigation, J. Constr. Steel Res. 54 (1) (2000) 109–133.
[33] L. Gardner, M. Ashraf, Structural design for non-linear metallic materials, Eng. Struct. 28 (6) (2006) 926–934.
[34] I. Arrayago, E. Real, L. Gardner, Description of stress–strain curves for stainless steel alloys, Mater. Des. 87 (2015) 540–552.
[35] X Yun, Z. Wang, L. Gardner, Full-range stress-strain curves for aluminum alloys, J. Struct. Eng., ASCE 147 (6) (2021) 04021060.
[36] Y.M. Wang, T. Voisin, J.T. McKeown, J. Ye, N.P. Calta, Z. Li, Z. Zeng, Y. Zhang, W. Chen, T.T. Roehling, R.T. Ott, M.K. Santala, P.J. Depond, M.J. Matthews, A. V. Hamza, T. Zhu, Additively manufactured hierarchical stainless steels with high strength and ductility, Nat. Mater. 17 (1) (2018) 63–71.
[37] S. Dryepondt, P. Nandwana, P. Fernandez-Zelaia, F. List III, Microstructure and high temperature tensile properties of 316L fabricated by laser powder-bed fusion, Addit. Manuf. 37 (2021) 101723.
[38] F. Bartolomeu, M. Buciumeanu, E. Pinto, N. Alves, O. Carvalho, F.S. Silva, G. Miranda, 316L stainless steel mechanical and tribological behavior—A comparison between selective laser melting, hot pressing and conventional casting, Addit. Manuf. 16 (2017) 81–89.
[39] Y. Zhong, L. Liu, S. Wikman, D. Cui, Z. Shen, Intragranular cellular segregation network structure strengthening 316L stainless steel prepared by selective laser melting, J. Nucl. Mater. 470 (2016) 170–178.
[40] N. Hadjipantelis, B. Weber, C. Buchanan, L. Gardner, Description of anisotropic material response of wire and arc additively manufactured thin-walled stainless steel elements, Thin-Walled Struct. 171 (2022) 108634.
[41] M.W. Wu, S.W. Ku, H.W. Yen, M.H. Ku, S.H. Chang, K. Ni, Z.S. Shih, C. Tsai, T. W. Hsu, C.L. Li, C.K. Wang, The synergic effects of heat treatment and building direction on the microstructure and anisotropic mechanical properties of laser powder bed fusion Corrax maraging stainless steel, Mater. Sci. Eng. 887 (2023) 145744.
[42] R. Fang, N. Deng, H. Zhang, G. Wang, Y. Su, H. Zhou, K. Gao, L. Gu, Effect of selective laser melting process parameters on the microstructure and properties of a precipitation hardening stainless steel, Mater. Des. 212 (2021) 110265.
[43] D. Dong, C. Chang, H. Wang, X. Yan, W. Ma, M. Liu, S. Deng, J. Gardan, R. Bolot, H. Liao, Selective laser melting (SLM) of CX stainless steel: Theoretical calculation, process optimization and strengthening mechanism, J. Mater. Sci. Technol. 73 (2021) 151–164.
[44] M. Sanjari, M. Mahmoudiniya, H. Pirgazi, S. Tamimi, M.H. Ghoncheh, A. Shahriairi, A. Hadadzadeh, B.S. Amirkhiz, M. Purdy, E.G. de Araujo, L. Kestens, M. Mohammadi, Microstructure, texture, and anisotropic mechanical behavior of selective laser melted maraging stainless steels, Mater. Charact. 192 (2022) 112185.
[45] S. Afkhami, V. Javaheri, E. Dabiri, H. Piili, T. Björk, Effects of manufacturing parameters, heat treatment, and machining on the physical and mechanical properties of 13Cr10Ni1.7Mo2Al0.4Mn0.4Si steel processed by laser powder bed fusion, Mater. Sci. Eng. 832 (2022) 142402.
[46] ASTM International (American Society for Testing and Materials) (2017). Standard guide for preparation of metallographic specimens. ASTM E3-11:*2017*, West Conshohocken, PA.

[47] ASTM International (American Society for Testing and Materials) (2007). Standard practice for microetching metals and alloys, ASTM E407-07:*2007*, West Conshohocken, PA.
[48] Bruker (2018), Quantax Esprit 2.2 [Computer software].
[49] F. Bachmann, R. Hielscher, H. Schaeben, Texture analysis with MTEX–free and open source software toolbox, Solid State Phenomena 160 (2010) 63–68.
[50] M.S. Pham, B. Dovgyy, P.A. Hooper, C.M. Gourlay, A. Piglione, The role of side-branching in microstructure development in laser powder-bed fusion, Nat. Commun. 11 (1) (2020) 1–12.
[51] M. Bahshwan, C.W. Myant, T. Reddyhoff, M.S. Pham, The role of microstructure on wear mechanisms and anisotropy of additively manufactured 316L stainless steel in dry sliding, Mater. Des. 196 (2020) 109076.
[52] ASTM E2627-23, Standard Practice for Determining Average Grain Size Using Electron Backscatter Diffraction (EBSD) in Fully Polycrystalline Materials, ASTM International, West Conshohocken, PA, 2013. Technical Report.
[53] Z. Hu, S. Gao, L. Zhang, X. Shen, H.L. Seet, S.M.L. Nai, J. Wei, Micro laser powder bed fusion of stainless steel 316L: cellular structure, grain characteristics, and mechanical properties, Mater. Sci. Eng. 848 (2022) 143345.
[54] D.J. Kotecki, T.A. Siewert, WRC-1992 constitution diagram for stainless steel weld metals: a modification of the WRC-1988 diagram, Weld J. 71 (5) (1992) 171–178.
[55] B. Almroth, Postbuckling behavior of orthotropic cylinders under axial compression, AIAA J. 2 (10) (1964) 1795–1799.
[56] CEN (European Committee for Standardization). (2017). Eurocode 3 - Design of steel structures, Part 1-6: Strength and Stability of Shell Structures. EN 1993-1-6: 2007+A1:2017, Brussels, Belgium.
[57] FARO (2018), FARO 8-Axis Design ScanArm 2.0.
[58] 3D Systems, Inc. (2017), Geomagic Wrap 2017 [Computer software].
[59] Robert McNeel & Associates, Rhino 7, https://www.rhino3d.com/, Version 7.
[60] B.W. Schafer, T. Peköz, Computational modeling of cold-formed steel: characterizing geometric imperfections and residual stresses, J. Constr. Steel Res. 47 (3) (1998) 193–210.
[61] B.W. Schafer, M. Grigoriu, T. Peköz, A probabilistic examination of the ultimate strength of cold-formed steel elements, Thin-Walled Struct. 31 (4) (1998) 271–288.
[62] Centre for Advanced Structural Engineering, Compression Tests of Stainless Steel Tubular Columns, University of Sydney, Sydney, NSW, Australia, 1990. *Investigation Report S770*.
[63] A.I. Osofero, M.A. Wadee, L. Gardner, Experimental study of critical and post-buckling behaviour of prestressed stayed columns, J. Constr. Steel Res. 79 (2012) 226–241.
[64] H.X. Yuan, Y.Q. Wang, L. Gardner, Y.J. Shi, Local–overall interactive buckling of welded stainless steel box section compression members, Eng. Struct. 67 (2014) 62–76.
[65] W. Mason, Mild-steel tubes in compression and under combined stress, Proc. Inst. Mech. Eng. 77 (1) (1909) 1205–1236.
[66] A. Robertson, The strength of tubular struts, Proc. R. Soc. Lond. Ser. A, Contain. Pap. Math. Phys. Character 121 (788) (1928) 558–585.
[67] S. Kanemitsu, N.M. Nojima, Axial Compression Test of Thin Circular Cylinders. A. Length Effect. B. Visual Study of Buckling, California Institute of Technology, 1939.
[68] Goree, W.S., & Nash, W.A. (1962). Elastic stability of circular cylindrical shells stabilised by a soft elastic core.
[69] J.C. Shang, W.J. Marulic, R.G. Sturm, Buckling of longitudinally stiffened cylinders, J. Struct. Div. 90 (5) (1964) 161–195.
[70] Thompson, L.E. (1965). Effects of internal pressure upon the buckling of thin circular cylindrical shells under axial compression.
[71] B. Ross, N.J. Hoff, W.H. Horton, The buckling behavior of uniformly heated thin circular cylindrical shells: an experimental investigation is undertaken to provide design-stability data for uniformly heated, clamped, thin circular cylindrical shells, Exp. Mech. 6 (1966) 529–537.
[72] L.R. Guist, Buckling Load of Thin Circular Cylindrical Shells Formed by Plastic Expansion, National Aeronautics and Space Administration, 1971.
[73] W.F. Chen, D.A. Ross, Tests of fabricated tubular columns, J. Struct. Div. 103 (3) (1977) 619–634.
[74] C.D. Miller, Buckling of axially compressed cylinders, J. Struct. Div. 103 (3) (1977) 695–721.
[75] M.A. Marzullo, A.A. Ostapenko, Tests on two high-strength shori tubular columns, in: Offshore Technology Conference, OTC, 1978 (pp. OTC-3086).
[76] Ostapenko, A., & Grimm, D.F. (1980). Local buckling of cylindrical tubular columns made of a-36 steel.
[77] Sobel, L.H., & Newman, S.Z. (1980). Plastic buckling of cylindrical shells under axial compression.
[78] Stephens, M.J., Kulak, G.L., & Montgomery, C.J. (1982). Local buckling of thin walled tubular steel members.
[79] W.D. Verduyn, I. Elishakoff, A Testing Machine for Statistical Analysis of Small Imperfect Shells: Part I, Delft University of Technology, Department of Aerospace Engineering, 1982. Report LR-357.
[80] G.D. Galletly, K. Pemsing, Interactive buckling tests on cylindrical shells subjected to axial compression and external pressure—A comparison of experiment, theory and various codes, Proc. Inst. Mech. Eng., Part C 199 (4) (1985) 259–280.
[81] Galletly, G.D., James, S., Kruzelecki, J., & Pemsing, K. (1987). Interactive buckling tests on cylinders subjected to external pressure and axial compression.
[82] P. Knoedel, T. Ummenhofer, U. Schulz, On the modelling of different types of imperfections in silo shells, Thin-Walled Struct. 23 (1–4) (1995) 283–293.
[83] P.A. Berry, J.M. Rotter, R.Q. Bridge, Compression tests on cylinders with circumferential weld depressions, J. Eng. Mech. 126 (4) (2000) 405–413.
[84] T.A. Winterstetter, H. Schmidt, Stability of circular cylindrical steel shells under combined loading, Thin-Walled Struct. 40 (10) (2002) 893–910.
[85] K. Athiannan, R. Palaninathan, Experimental investigations on buckling of cylindrical shells under axial compression and transverse shear, Sadhana 29 (2004) 93–115.
[86] K. Kalnins, M.A. Arbelo, O. Ozolins, E. Skukis, S.G. Castro, R. Degenhardt, Experimental nondestructive test for estimation of buckling load on unstiffened cylindrical shells using vibration correlation technique, Shock Vib. 2015 (1) (2015) 729684.
[87] F. Aslani, B. Uy, J. Hur, P. Carino, Behaviour and design of hollow and concrete-filled spiral welded steel tube columns subjected to axial compression, J. Constr. Steel Res. 128 (2017) 261–288.
[88] L. Guo, Y. Liu, H. Jiao, S. An, Behavior of thin-walled circular hollow section stub columns under axial compression, Int. J. Steel Struct. 16 (2016) 777–787.
[89] O. Zhao, L. Gardner, B. Young, Structural performance of stainless steel circular hollow sections under combined axial load and bending—Part 1: experiments and numerical modelling, Thin-Walled Struct. 101 (2016) 231–239.
[90] A. Gorbachov, N. Stranghöner, J.M. Rotter, 04.03: buckling behaviour of axially compressed cylindrical shells made of stainless steel, CE/Papers 1 (2–3) (2017) 828–837.
[91] P. Jiao, Z. Chen, X. Tang, W. Su, J. Wu, Design of axially loaded isotropic cylindrical shells using multiple perturbation load approach—Simulation and validation, Thin-Walled Struct. 133 (2018) 1–16.
[92] D. Li, B. Uy, F. Aslani, C. Hou, Behaviour and design of spiral-welded stainless steel tubes subjected to axial compression, J. Constr. Steel Res. 154 (2019) 67–83.
[93] X. Meng, L. Gardner, Cross-sectional behaviour of cold-formed high strength steel circular hollow sections, Thin-Walled Struct. 156 (2020) 106822.
[94] F.J. Bridget, C.C. Jerome, A.B. Vosseller, Some new experiments on buckling of thin-wall construction, Trans. Am. Soc. Mech. Eng. 56 (6) (1934) 569–578.
[95] L.H. Donnell, A new theory for the buckling of thin cylinders under axial compression and bending, Trans. Am. Soc. Mech. Eng. 56 (8) (1934) 795–806.
[96] Osgood, W.R. (1938). *The crinkling strength and the bending strength of round aircraft tubing* (No. NACA-TR-632).
[97] L.A. Harris, H.S. Suer, W.T. Skene, R.J. Benjamin, The stability of thin-walled unstiffened circular cylinders under axial compression including the effects of internal pressure, J. Aeronaut. Sci. 24 (8) (1957) 587–596.
[98] W.H. Horton, S.C. Durham, The Effect of Restricting Buckle Depth in Circular Cylindrical Shells Repeatedly Compressed to the Buckling Limit, Department of Aeronautics and Astronautics, Stanford University, 1963, p. 0020.
[99] O. Steinhardt, U. Schulz, Zum beulverhalten von kreiszylinderschalen, Schweizerische Bauzeitung 89 (1) (1971) 1–14.
[100] Lundquist, E.E. (1934). *Strength tests of thin-walled duralumin cylinders in compression* (No. NACA-TR-473).
[101] Holt, M. (1941). Tests on Stiffened Circular Cylinders (No. NACA-TN-800).
[102] J.W. Clark, M. Holt, Effect of imperfections on buckling of thin cylinders and columns under axial compression, J. Appl. Mech. 17 (3) (1950) 340–341.
[103] Lo, H., Crate, H., & Schwartz, E.B. (1951). Buckling of thin-walled cylinder under axial compression and internal pressure (No. NACA-TR-1027).
[104] R.L. Moore, Torsion, Compression, and Bending Tests of Tubular Sections Machines from 75S-T6 Rolled Round Rod, National Advisory Committee for Aeronautics, 1952.
[105] Peterson, J.P., & Dow, M.B. (1959). Compression tests on circular cylinders stiffened longitudinally by closely spaced Z-section stringers (No. NASA-MEMO-2-12-59L).
[106] M.B. Dow, J.P. Peterson, Bending and Compression Tests of Pressurized Ring-Stiffened Cylinders, 360, National Aeronautics and Space Administration, 1960.
[107] J.W. Clark, R.L. Rolf, Design of aluminum tubular members, J. Struct. Div. 90 (6) (1964) 259–289.
[108] S.C. Batterman, Plastic buckling of axially compressed cylindrical shells, AIAA J. 3 (2) (1965) 316–325.
[109] A.N. Sherbourne, R.M. Korol, Buckling of cylindrical shells under axial compression, J. Struct. Div. 93 (5) (1967) 29–51.
[110] D. Fitzgibbon, Preliminary Results of Sub-Scale Tests on Cylinders Filled with an Elastic Core (1960). GM-60-7520.6-11.
[111] B.O. Almroth, A.M.C. Holmes, Buckling of shells with cutouts, experiment and analysis, Int. J. Solids Struct. 8 (8) (1972) 1057–1071.
[112] M.C. Lin, M.K. Yeh, Buckling of elastoplastic circular cylindrical shells under axial compression, AIAA J. 32 (11) (1994) 2309–2315.
[113] R. Sliž, M.Y. Chang, Reliable and accurate prediction of the experimental buckling of thin-walled cylindrical shell under an axial load, Thin-Walled Struct. 49 (3) (2011) 409–421.
[114] W Ballerstedt, H. Wagner, Versuche über die Festigkeit dünner unversteifter Zylinder unter Schub-und Längskräften, Luftfahrtforschung 13 (9) (1936) 309–312.
[115] N.J. Hoff, T. Von Kármán, Buckling of Thin Shells (No. 114), Department of Aeronautical Engineering, Stanford University, 1961.
[116] C.D. Babcock, E.E. Sechler, *The Effect of Initial Imperfections on the Buckling Stress of Cylindrical Shells* (No. NASA-TN-D-2005), National Aeronautics and Space Administration, 1963.
[117] C.D Babcock Jr., The influence of the testing machine on the buckling of cylindrical shells under axial compression, Int. J. Solids. Struct. 3 (5) (1967) 809–817.
[118] J. Arbocz, C.D Babcock Jr., The effect of general imperfections on the buckling of cylindrical shells, J. Appl. Mech. 36 (1) (1969) 28–38.

[119] W.H. Horton, S.C. Durham, Imperfections, a main contributor to scatter in experimental values of buckling load, Int. J. Solids Struct. 1 (1) (1965) 59–72.
[120] Sendelbeck, R.L., Carlson, R.L., & Hoff, N.J. (1967). An experimental study of the effect of length on the buckle pattern of axially compressed circular cylindrical shells (Vol. 67, No. 1981). Air Force Office of Scientific Research, Air Research and Development Command, United States Air Force.
[121] D.R. Shover, On the Problem of Geometrical Imperfections in Thin Circular Cylindrical Shells, Stanford University, 1968.
[122] R.S. Sendelbeck, N.J. Hoff, Loading rig in which axially compressed thin cylindrical shells buckle near theoretical values: a holding and alignment test rig for use when buckling thin circular cylindrical shells is described. The consistency of high buckling values is demonstrated along with results concerning different holding restrictions, Exp. Mech. 12 (1972) 372–376.
[123] SIMULIA - Dassault Syst`emes (2022), Abaqus 2022 [Computer software].
[124] M. Theofanous, T.M. Chan, L. Gardner, Flexural behaviour of stainless steel oval hollow sections, Thin-Walled Struct. 47 (6-7) (2009) 776–787.
[125] H.X. Yuan, Y.Q. Wang, L. Gardner, Y.J. Shi, Local–overall interactive buckling of welded stainless steel box section scompression members, Eng. Struct. 67 (2014) 62–76.
[126] O. Zhao, B. Rossi, L. Gardner, B. Young, Experimental and numerical studies of ferritic stainless steel tubular cross sections under combined compression and bending, J. Struct. Eng. 142 (2) (2016) 04015110.
[127] M. Kucukler, L. Gardner, L. Macorini, Lateral–torsional buckling assessment of steel beams through a stiffness reduction method, J. Constr. Steel Res. 109 (2015) 87–100.
[128] P. Kyvelou, L. Gardner, D.A. Nethercot, Finite element modelling of composite cold-formed steel flooring systems, Eng. Struct. 158 (2018) 28–42.
[129] F. Walport, L. Gardner, E. Real, I. Arrayago, D.A. Nethercot, Effects of material nonlinearity on the global analysis and stability of stainless steel frames, J. Constr. Steel Res. 152 (2019) 173–182.